Energetic Electron Tail Production from Binary Encounters of Discrete Electrons and Ions in a Sub-Dreicer Electric Field

Paul M. Bellan

Applied Physics and Material Science, Caltech, Pasadena CA 91125 USA

(*Author to whom correspondence should be addressed:pbellan@caltech.edu)

(Dated: 2 September 2023)

During transient instabilities in a 2 eV, highly-collisional MHD-driven plasma jet experiment, evidence of a 6 keV electron tail was observed via x-ray measurements. The cause for this unexpected high-energy tail is explored using numerical simulations of the Rutherford scattering of a large number of electrons and ions in the presence of a uniform electric field that is abruptly turned on as in the experiment. When the only active processes are Rutherford scattering and acceleration by the electric field then, contrary to the classical Fokker-Planck theory of plasma resistivity, it is found that no steady-state develops and instead, the particle kinetic energy increases continuously. However, when a power loss mechanism is introduced mimicking atomic line radiation, then a near steady-state can develop and, in this case, an energetic electron tail similar to that observed in the experiment can develop. The reasons underlying this behavior are analyzed and it is shown that an important consideration is that Rutherford scattering is dominated by the cumulative effect of grazing collisions whereas atomic line radiation requires an approximately direct rather than a grazing collision.

I. INTRODUCTION

A. Motivation

This paper is motivated by unexpected observations of short bursts of 6 keV X-rays¹ in the Caltech MHD plasma jet experiment. These bursts were unexpected because the combination of low plasma temperature and high density made the plasma highly collisional so it seemed impossible for an electron to accelerate to attain the 6 keV kinetic energy required to produce 6 keV X-rays. A previous model² sought to explain these observations, but while aspects of this previous model were compelling, there were also serious shortcomings. This paper presents a new model which has been constructed to overcome these shortcomings. Previous related literature was surveyed to put the new model in context; the results of this survey will now be summarized with additional details given in Appendix A. In addition, comparison to selected aspects of previous work will be given throughout the body of the paper. While the model presented here was motivated by a desire to explain the surprising observations in the Caltech jet experiment, it is expected that the methodology and the results should have wider applicability than just the Caltech jet experiment. This is because high energy tails and energetic particles are observed in many different plasma contexts such as the solar corona³, the solar wind⁴, astrophysical situations⁵, and tokamaks⁶.

B. Comparison of collisions in neutral gas to collisions in plasma

In a neutral gas consisting of identical particles the situation is quite simple: collisions between the particles cause the velocity distribution to become Maxwellian in the rest frame of the center of mass and there is no interaction with an imposed electric field.

In contrast, the corresponding situation in a plasma with an imposed electric field is quite complicated. Plasmas contain two types of particles, electrons and ions with very different masses. The electrons and ions are accelerated in opposite directions at different rates by the electric field. Furthermore, there are four types of collisions: electron-electron, electron-ion, ion-electron, and ion-ion collisions (denoted e-e, e-i, i-e, and i-i) and the momentum and energy transfer rates for these four types differ.

As a result of this complexity, unlike a neutral gas, plasmas frequently exhibit non-Maxwellian distributions, most particularly high energy electron tails. Many models and mechanisms have been proposed to explain these tails. Examples³ of proposed mechanisms are direct DC accel-

eration, coherent wave acceleration, turbulent acceleration, and shock acceleration. Which of these mechanisms dominates depends on the specific situation. Mechanisms other than direct DC acceleration are typically based on the assumption that the plasma is collisionless whereas DC acceleration models typically consider the competition between frictional drag from collisions and the acceleration provided by the electric field.

Because the duration of the X-ray bursts observed in the Caltech experiment is very short compared to the experiment duration, it is presumed that a transient analysis is required. Furthermore, the burst duration is so short that there is insufficient time for either coherent or turbulent waves to develop. Thus, it is assumed here that the X-ray bursts are a result of DC acceleration provided by a very large, but short-lived electric field. A possible origin for this electric field is given in Zhou and Bellan where it is proposed that the short-duration, large electric field develops as a result of the MHD-driven plasma jet developing a cascading sequence of qualitatively different instabilities where each instability in the sequence destabilizes the next. The kinking of the MHD-driven jet is the primary instability and this involves a rapid lateral acceleration that produces an effective gravity that enables a Rayleigh-Taylor instability which is the secondary instability 10. The periodic ripples of the Rayleigh Taylor instability constrict the jet current channel and this leads to the tertiary instability which is a collisional version of the Buneman instability 11. The Buneman-like instability enables production of a large transient electric field which for the purposes of particle acceleration can be considered as an abruptly-imposed large DC electric field.

Because frictional drag in a plasma decreases with particle kinetic energy, a sufficiently energetic electron experiences negligible drag. Such an electron can run away and become effectively collisionless, leaving behind the lower energy collisional electrons. All electrons run away for a sufficiently large electric field, called the Dreicer¹² field E_D where

$$E_D = 0.43 \frac{ne^3}{8\pi\varepsilon_0^2 \kappa T_e} \ln \Lambda. \tag{1}$$

Here $\ln \Lambda$ is called the Coulomb logarithm where $\Lambda = \lambda_D/b_{\pi/2}$, λ_D is the Debye length and $b_{\pi/2}$ is the 90 degree impact parameter for Rutherford scattering. These issues have been studied in tokamak, solar, and astrophysical contexts for over seventy years and have resulted in thousands of papers so it is only possible to cite a few. The models proposed in these papers inevitably invoke assumptions, these models have different degrees of complexity, and several competing effects interact. While it is generally straightforward to model how individual effects work, when all effects are simultaneously active, synergistic interactions can develop that are not easily modeled. Ex-

amples of the consequences of individual effects are: (1) e-e collisions tend to create Maxwellian velocity distributions in the electron rest frame, (2) e-i collisions tend to make the electron velocity distribution function isotropic with respect to the ion center of mass velocity – a different definition of isotropic from the definition associated with e-e collisions, (3) if collisions are unimportant, the electric field shifts the entire electron velocity distribution in the acceleration direction with no change in the profile of the velocity distribution, and (4) e-i collisions tend to heat both electrons and ions with most of the heating going to the electrons. When these effects and some others are all simultaneously occurring, it is not immediately obvious how they combine. In particular it is not immediately obvious whether effect (1) or effect (2) dominates since these two effects have different results. This is because when there is an electric current, an electron velocity distribution being isotropic in the electron center of mass frame differs from being isotropic in the ion center of mass frame.

Table I is a matrix summarizing how the new model relates to representative previous models. This table lists assumptions inherent in the previous models and, in the right-most column, assumptions made in the new model. This right-most column indicates that the significant differences are:

- 1. the new model does not always assume that Debye shielding is operative,
- 2. the new model uses a more detailed description of binary encounters than does the conventional approach involving differential cross-sections,
- 3. the nature of velocity distributions is not constrained so unlike previous models, the electron velocity distribution is not assumed to be the sum of a Maxwellian and a perturbation nor to be a shifted Maxwellian (definitions and discussions of these types of velocity distributions are given in Appendix A),
- 4. individual discrete particle encounters are calculated rather than some analytic model of the average effect of many encounters,
- 5. e-e, e-i, i-e, and i-i collisions are assumed to be interspersed rather than, for example, a large number of e-e collisions followed by a large number of e-i collisions,
- 6. both grazing and large-angle collisions are taken into account,
- 7. the solution is time-dependent,

- 8. there is no assumption of a heat bath¹³ imposing a constant electron temperature,
- 9. a realistic mechanism for shedding heat produced by Ohmic dissipation is discussed.

Appendix A provides a short review of both the "shifted Maxwellian" and "Maxwellian plus perturbation" methods used in previous models and notes issues with both of these approaches. Concepts discussed in Appendix A will be referred to in the main body of the paper.

Particle-in-cell codes^{14,15} typically use a collision model that is somewhat similar to the model presented here, but critical important differences exist that will be highlighted in the main body of the paper. Question marks have been placed in some of the entries for assumptions in Table I because the model proposed in Takizuka and Abe ¹⁴ and in Arber *et al.* ¹⁵ makes these assumptions in some parts of the development of their model but not in others; this will be discussed in the main body of the present paper. The reason question marks have been placed for the Braginskii ¹⁶ assumptions in Table I will be discussed in Appendix A.

II. CALTECH JET EXPERIMENT AND PREVIOUS MODEL FOR OBSERVATION OF X-RAYS IN THIS EXPERIMENT

The Caltech jet experiment and the model previously constructed to explain it will now be summarized. These issues are believed to be of much wider relevance than just the Caltech jet experiment, but referring to a specific experiment provides a tangible example.

A. Caltech Jet Experiment

Measured parameters for the Caltech experiment are listed in the top eight rows of Table II; parameters of the model to be discussed are listed in rows nine and below. The salient observation in the Caltech experiment is that a large, but sub-Dreicer, electric field accelerated a tiny fraction of the electrons to an extremely high energy. This is surprising because, at first sight, the high collisionality of the Caltech plasma would be expected to cause an electron to lose any directed energy gained from the electric field so the electron could never attain high energy. The initial electron temperature was 2 eV and the electron collision mean free path was $l_{mfp} = 1 \mu m$, a microscopic length compared to the several centimeter plasma dimensions. It was observed that a sequence of MHD instabilities in a 10 cm long plasma segment led to a 1 μ s burst of 6 keV X-rays. Since an X-ray is generated by electron acceleration or deceleration, the presence of these

Assumption	C	CSR	SH	Tr	Br	KT,Be	N	K	СН	LE	ТА	pp
cutoff log integral at interparticle distance, $n^{-1/3}$	Y											
cutoff log integral at Debye length		Y	Y	Y	Y	Y	Y	Y	Y	Y	Y	
differential cross section w/field particle flux	Y	Y	Y	Y	Y	Y		Y	Y	Y	?	
Maxwellian plus perturbation, $f_e = f_{Max} + f_1$	n/a	Y	Y		?		n/a	Y		Y	?	
Shifted Maxwellian, $f_e = n(\pi v_T)^{-3/2} e^{-(\mathbf{v} - \mathbf{u}_e)^2 / v_{Te}^2}$	n/a			Y	?	Y						
electron-ion collisions only	n/a	Y										
electron-electron and electron-ion collisions	n/a		Y	Y	Y	Y		Y	Y	Y	Y	Y
interspersed e-e, e-i, and i-e collisions	n/a										?	Y
both grazing and large angle collisions considered											?	Y
time-dependent solution											Y	Y
electron, ion temperatures can vary											Y	Y
explicit power loss mechanism incorporated												Y
individual discrete particle collisions evaluated											?	Y
relativistic									Y			

TABLE I. List of assumptions that have been made in previous models compared to assumptions in present paper model (right-most column). A "Y" denotes that the assumption has been made while a blank cell denotes that the assumption has not been made. A question mark denotes that the assumption has been made in some parts of the model but not in others. C=Chandrasekhar ¹⁷, CSR=Cohen *et al.* ¹⁸, SH=Spitzer and Härm ¹⁹, Tr=Trubnikov ²⁰, Br=Braginskii ¹⁶, KT=Krall and Trivelpiece ²¹, Be=Bellan ²², N=Nanbu ²³, K=Kulsrud *et al.* ¹³, CH=Connor and Hastie ²⁴, LE=Landreman and Ernst ²⁵, TA=Takizuka and Abe ¹⁴, pp= present paper

,

X-rays implied that a small fraction of electrons was accelerated to 6 keV in 10 cm, i.e., there must have been a transient electric field $E=6\times 10^4$ V/m. This transient electric field would have a duration corresponding to the duration of the X-ray burst, i.e., about 1 μ s. Since $d=at^2/2$ where $a=q_eE/m_e=10^{16}$ m s⁻² is the acceleration, the duration of this acceleration would be $t=\sqrt{2m_ed/(q_eE)}=4$ ns. The electrons would have been accelerated in this time to a directed velocity $eEt/m_e=4\times 10^7$ m/s, i.e., about 50 times larger than their initial thermal velocity of 8×10^5 m/s.

symbol Caltech Jet Expt

density (m ⁻³)	n	10 ²²
electron temperature (eV)	T_e	2
classical resistivity (Ohm-m)	η_0	2×10^{-4}
electron Debye length (m)	λ_{De}	10^{-7}
interparticle spacing (m)	$n^{-1/3}$	4.6×10^{-8}
transient electric field (V/m)	E	6×10^4
Dreicer electric field (V/m)	E_D	3×10^5
reference velocity (m s^{-1})	v_0	8.4×10^5
meta-Debye length (m)	λ_f	10^{-7}
$4\pi n\lambda_f^3$	Λ_f	146
$\frac{ne^3}{8\pi\varepsilon_0^2\mu_e v_0^2}$ (V/m)	E_0	6.5×10^4
normalized electric field	$ar{E}_z$	0.9
acceleration factor	$rac{ar{E}_z}{2\Lambda_f^2}$	2×10^{-5}

TABLE II. Caltech MHD jet experiment parameters

Multiple X-ray bursts have been recently been observed by Zhang *et al.* ²⁶ in an experiment involving similar parameters but having the geometry of a braided solar corona loop. Zhou and Bellan⁷ proposed that the instability producing the transient electric field is a highly-collisional variant of the two-stream (Buneman) instability.

B. Summary of possible explanation by Marshall and Bellan²

The mean free path is the distance electrons must travel to scatter 90 degrees; this scattering could be by any mechanism or combination of mechanisms. After traveling a mean free path, electrons would thus lose the directed velocity gained from the electric field. Because the mean free path resulting from Coulomb collisions is only 1 μ m and the system characteristic length is many orders of magnitude larger, electrons should never be able to attain the large velocity required to produce X-rays. Thus, the observation of X-rays in the Caltech experiment conflicts with expectations. A possible explanation for how a tiny fraction of electrons attained this large velocity was proposed by Marshall and Bellan². This explanation combined cross-section con-

cepts with the property that the classical plasma collision theory predicts that the mean free path for collisions of superthermal electrons with ions l_{mfp} scales as W^2 where W is the electron kinetic energy (the reason for this W^2 scaling is given at the end of Sec.IV). According to this explanation, an electron has a probability of $1 - e^{-1} \simeq 0.63$ for being scattered after traveling a distance l_{mfp} so the electron should have an $e^{-1} = 0.37$ probability of not being scattered on travelling l_{mfp} . Unscattered electrons would gain an energy $\Delta W = q_e E l_{mfp}$ and their associated directed momentum would not be lost. Because $\left(l_{mfp} + \Delta l_{mfp}\right)/l_{mfp} = \left(W + q_e E l_{mfp}\right)^2/W^2$ the mean free path would increase for these unscattered electrons so their mean free path on the next collision would be slightly larger. In the next collision again a fraction e^{-1} would not scatter and gain energy. The process would repeat, resulting in an increasing l_{mfp} and W for an ever-decreasing fraction of the electrons. Thus, there would be an e^{-N} fraction of electrons that had made N progressively larger mean free paths without scattering and these would have attained the required 6 keV energy after going 10 cm without scattering. Eventually, some of these energetic electrons would undergo a rapid deceleration via a large angle collision and so would generate X-rays via bremsstrahlung.

C. Shortcomings of the Marshall and Bellan explanation and of the Debye shielding argument

The Marshall and Bellan explanation summarized above has two shortcomings.

First, the Marshall and Bellan explanation is based on cross-sections, the concept that a particle either hits or misses a target. Here, e^{-1} constituted the fraction of electrons that missed hitting another particle. However, Coulomb scattering is not a hit-or-miss process but rather the result of a large number of binary interactions where each interaction produces a random deflection and the statistics of these deflections is such that the cumulative effect of weak deflections dominates that of occasional strong deflections. Thus, one cannot isolate a subset of electrons that do not scatter because all electrons are continuously being deflected by various amounts.

The second problem of the Marshall and Bellan explanation was the use of the Coulomb logarithm $\ln \Lambda$ where $\Lambda = \lambda_D/b_{\pi/2}$, λ_D is the Debye length, and $b_{\pi/2}$ is the 90 degree impact parameter. Thus $\ln \Lambda$ depends on Debye shielding which in turn depends on the presumption that electrons and ions have Maxwellian velocity distributions and an associated temperature. The problem is that the derivation of Debye shielding assumes that the dynamics of the binary interaction under consideration is sufficiently slow that enough time has elapsed for a Debye shielding cloud to be

established. As noted on p. 109 of Trubnikov 20 and in Trofimovich and Krainov 27 , the time required for a Debye shielding cloud to be established is $1/\omega_{pe}$ where ω_{pe} is the electron plasma frequency. The time for a particle having velocity v to traverse a Debye shielding cloud is λ_{De}/v . If this traversal time is shorter than the time for the Debye shielding cloud to become established, the Debye shielding cloud will not exist. The condition for there being insufficient time for a Debye shielding cloud to be established is thus $\lambda_{De}/v \ll 1/\omega_{pe}$ which can be re-arranged as

$$v \gg \omega_{pe} \lambda_{De} = \sqrt{\kappa T_e / m_e} \tag{2}$$

corresponding to the test particle being superthermal. Thus, the Coulomb logarithm $\ln \Lambda$ is not applicable to superthermal particles.

This conclusion can be understood in an equivalent manner as follows. For each binary encounter between a given test particle T and a Debye-shielded specific field particle F, all particles in the plasma other than T and F must have sufficient time to arrange themselves to form a Debye shielding cloud around the field particle F. This is clearly impossible if the process occurs faster than the time required for shielding particles to make the required displacement to come into position to do their shielding job. A well-known example of this constraint is that ion shielding clouds do not form around electrons because, being slow, ions cannot keep up with electrons. Another example is a calculation by Nicholson²⁸ who showed that a slow-moving particle has a Debye shielding cloud but this disappears when the particle velocity becomes superthermal. This means that the use of the Coulomb logarithm $\ln \Lambda$, a quantity intrinsic to the classic theory and depending on Debye shielding being operative, is inappropriate for describing test particles moving faster than all other particles.

III. SUMMARY OF THE NEW MODEL

The first main result is to show via direct numerical calculation of all binary encounters of a large number of electrons and ions in a suddenly-applied, macroscopic, uniform, constant electric field that a steady-state does not develop. By "all" it is meant that both small-angle and large-angle deflections are taken into account with no a-priori assumption about relative weighting; the greater effect of small-angle collisions develops as a result of the numerical calculation rather than from being imposed as a result of analytic arguments. The second main result is to show that a quasi-steady-state can be achieved by modifying the system to have a power loss mechanism; this

mechanism is related to the heat bath assumed by Kulsrud¹³, but involves a less constraining assumption because the mechanism does not impose an arbitrary fixed temperature. The imposition of a power loss mechanism leads to a non-uniqueness because different forms of power loss are possible. A realistic loss mechanism that is explored in detail here invokes atomic line radiation. This is accomplished by allowing for certain electrons to make inelastic collisions with ions. These inelastic collisions occur if a suitably energetic electron makes a nearly head-on collision with an ion and so it is important that the possibility of infrequent large-angle collisions has been allowed. In such a near head-on collisions the ion is excited to a higher quantum energy state and then nearly immediately emits a photon that carries away the energy the ion absorbed in the inelastic collision. The inelastically colliding electron also transfers momentum to the ion in an amount that conserves overall momentum. This atomic line radiation model provides insights regarding how the power injected via Ohmic dissipation is balanced by a realistic power loss mechanism. The details show that a tail of energetic electrons can be generated by this process.

IV. RELEVANT CONCEPTS IN CLASSICAL THEORY

Certain basic concepts of the classical theory are now summarized so that issues with these familiar concepts can be identified and discussed:

1. A charged particle of species σ is surrounded by a Debye shielding cloud so that its electrostatic potential is given by

$$\phi(\mathbf{r}) = \frac{q_{\sigma}}{4\pi\varepsilon_0 r} e^{-r/\lambda_D} \tag{3}$$

where λ_D is the Debye length.

2. The Debye length is defined as

$$\frac{1}{\lambda_D^2} = \frac{1}{\lambda_{D_i^2}} + \frac{1}{\lambda_{D_e^2}} \tag{4}$$

where

$$\lambda_{D\sigma}^2 = \frac{\varepsilon_0 \kappa T_{\sigma}}{ne^2} \tag{5}$$

and the plasma is assumed to be macroscopically quasi-neutral so $n_i = n_e = n$.

- 3. There is a large number of particles in a Debye sphere, i.e., $n\lambda_D^3 \gg 1$.
- 4. Collisions consist of encounters between two particles at a time; i.e., there are no encounters where three or more particles mutually interact. These two-particle encounters, called binary

encounters, are described in the center of mass frame of the two particles. The classical collision theory considers a fictitious particle having reduced mass μ moving at the relative velocity

$$\mathbf{v} = \mathbf{v}_T - \mathbf{v}_F \tag{6}$$

where \mathbf{v}_T and \mathbf{v}_F are the respective initial velocities of the colliding test (T) and field (F) particles and the reduced mass μ is defined as

$$\frac{1}{\mu} = \frac{1}{m_T} + \frac{1}{m_F}.\tag{7}$$

The collision dynamics are mapped to that of a fictitious particle of mass μ scattering from a fixed scattering center with a resulting deflection by an angle θ ; the scattering geometry is sketched in Fig.1. The Rutherford scattering formula summarizes the solution to the dynamics and gives the scattering angle θ via

$$\tan\left(\frac{\theta}{2}\right) = \frac{q_T q_F}{4\pi\varepsilon_0 b\mu v^2}.\tag{8}$$

Here b is the impact parameter as sketched in Fig.1. The magnitude of ${\bf v}$ does not change during the collision so the collision can be pictured as a rotation of ${\bf v}$ by the angle θ in the plane of the sketch. Equation 8 defines a special impact parameter $b_{\pi/2}$, called the 90-degree impact parameter, which is the impact parameter for which $\theta=\pi/2$; thus $b_{\pi/2}=q_Tq_F/(4\pi\epsilon_0\mu v^2)$.

5. The number of binary encounters in a time Δt for each differential scattering cross section $d\sigma = bdbd\phi$ is calculated where ϕ is the azimuthal angle about the initial direction of the relative velocity. The number of such binary encounters during the time Δt is given by the volume swept out by the relative velocity in the time Δt times the density of field particles, i.e., the number of these encounters is $n_F d\sigma v \Delta t$. This differential scattering cross section picture inherently assumes that an electron makes a long sequence of binary encounters with either just ions or just electrons where the impact parameter in each encounter of this sequence is the same, and that the electron continues in the same direction after each binary encounter despite, in fact, being deflected. Thus, the counting of binary encounters in the differential cross-section picture does not describe the true situation that after an electron has had a binary encounter with another electron, the electron may next have a binary encounter with an ion or with another electron, i.e., that the encounters with electrons and ions are, in reality, interspersed. This is important because when an electron collides with another electron, both the energy and momentum of the incident electron change but when an electron collides with an ion, only momentum of the incident electron changes (to the extent that the ion is infinitely heavy).

6. The cumulative effect of small angle collisions dominates over the cumulative effect of large angle collisions and for small angle collisions

$$\theta = \frac{q_T q_F}{2\pi \varepsilon_0 b \mu v^2}.\tag{9}$$

- 7. The reduction of velocity in the direction of v scales as θ^2 and so is proportional to $1/(b^2v^4)$.
- 8. Multiplying the reduction in velocity per encounter by the number of encounters in time Δt gives the reduction in velocity in time Δt to scale as $n_F \Delta t d\sigma/(b^2 v^3)$.
- 9. Integrating over all possible impact parameters $d\sigma = bdbd\phi$ results in a logarithmically singular integral of the form $\int b^{-1}db$ which leads to an issue of how to choose the lower and upper bounds of this integral. The issue is resolved by assuming that the lower bound is the impact parameter at which $\theta = \pi/2$ while the upper bound is the Debye length so that $\int b^{-1}db = \ln(\lambda_D/b_{\pi/2})$. The lower limit is set on the grounds that collisions with $\theta \geq \pi/2$ are unimportant relative to the cumulative effect of the much more numerous collisions having $\theta \ll \pi/2$ while the upper limit is chosen by invoking Eq.3 to state that the interaction electric field vanishes when the test and field particles are separated by more than a Debye length.

For purposes of calculating electrical resistivity, it is assumed that the electron temperature determines the Debye length and that $\mu v^2 = \kappa T_e$ in Eq.8 so

$$\frac{1}{b_{\pi/2}} = 4\pi n \lambda_D^2 \tag{10}$$

and

$$\ln\left(\frac{\lambda_D}{b_{\pi/2}}\right) = \ln\left(4\pi n \lambda_D^3\right). \tag{11}$$

Because of the logarithmic dependence in Eq.11, it is presumed that the precision with which $n\lambda_D^3$ is calculated is not critical. Questions arise immediately regarding the physical meaning of using Debye shielding together with Eq.8 because Eq.8 describes a fictitious reduced-mass particle scattering from a scattering center fixed in the center of mass frame. It is not obvious how the lab-frame motion of real electrons and ions as assumed in the screening argument applies to the fictitious scattering center fixed in the center of mass frame; that is, it is not clear what real particles are shielding the fictitious scattering center. The Debye shielding derivation involves a test particle that is a real particle, not a fictitious particle.

If just electrons colliding with ions is considered, it is assumed that the electron temperature determines the Debye length, and integration over impact parameters predicts an electron-ion collision frequency $v_{ei} = \frac{ne^4 \ln \Lambda}{4\pi\epsilon_0^2 m_e^2 v^3}$ (see Eq.11.16 of Goldston and Rutherford ²⁹).

Since the mean free path for an electron having velocity v is $v\tau_{ei}$, where $\tau_{ei} = 1/v_{ei}$, it is seen that the mean free path scales as v^4 , that is as W^2 where W is the electron kinetic energy. This W^2 scaling was used in the Marshall and Bellan model summarized in Sec.II B.

A balance between acceleration from the **E** field and collisional drag results in an electric current density

$$\mathbf{J} = ne(\mathbf{u}_i - \mathbf{u}_e) \tag{12}$$

that is related to E by Ohm's law

$$\mathbf{E} = \eta \mathbf{J} \tag{13}$$

where for singly charged ions, the electrical resistivity η is

$$\eta = \frac{e^2 m_e^{1/2}}{3\sqrt{\pi}\pi\varepsilon_0^2} \frac{\ln\Lambda}{(2\kappa T_e)^{3/2}}$$
 (14)

and $\ln \Lambda$, the Coulomb logarithm, is of order 10.

The resistivity η is determined via a Fokker-Planck¹⁷ model that sums the consequence of transient microscopic electric fields that particles experience when in close proximity to each other.

V. PROBLEMS WITH ASSUMING A STEADY-STATE

There is a logical inconsistency in the classical model assumption that an isolated system in a constant uniform electric field develops a steady state. Resistivity causes dissipative heating $\eta J^2 = E^2/\eta$. Kulsrud¹³ explicitly acknowledged this heating issue and in his modeling, stated that the plasma was immersed in a heat bath that forced the temperature to remain constant. However, if no heat bath is assumed, there will be heating of the plasma because of the resistive dissipation. Initially, this dissipation mainly heats electrons so

$$\frac{d}{dt}\left(\frac{3}{2}n\kappa T_e\right) = \frac{E^2}{\eta}.\tag{15}$$

Since the density n is assumed constant in time, Eq.15 shows that it is inconsistent to assume that an isolated plasma (i.e., no heat bath) develops a constant T_e in the presence of an electric field. Furthermore, if as predicted by the classical theory, the resistivity scales as $\eta = \eta_0 (T_0/T_e)^{3/2}$, then Eq.15 can be integrated to give

$$\frac{T_e(t)}{T_{e,0}} = \left(1 - \frac{E^2/\eta_0}{3n\kappa T_{e,0}}t\right)^{-2} \tag{16}$$

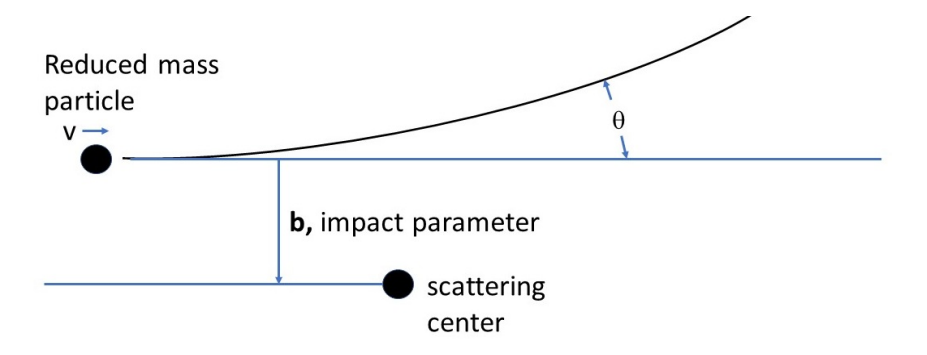


FIG. 1. Rutherford scattering geometry

which is a faster-than-exponential growth rate producing an infinite temperature in the finite time $t_{\infty} = 3n\kappa T_{e,0}\eta_0/E^2$. The time for the temperature to quadruple from its initial value is $t_{4\times} = 3n\kappa T_{e,0}\eta_0/2E^2$. Using Eqs. 1 and 14 and ignoring coefficients of order unity, the quadrupling time can be expressed as

$$t_{4x} \sim \frac{(E_D/E)^2}{v_{ei}}.$$
 (17)

where the electron-ion collision frequency v_{ei} is given by

$$v_{ei} \sim \frac{\omega_{pe}}{n\lambda_D^3} \ln \Lambda.$$
 (18)

Since v_{ei}^{-1} is typically a very small fraction of a plasma lifetime, the quadrupling time will be short compared to the plasma lifetime if E_D/E is not extremely large. The results in Eqs.16-17 are only accurate to within a factor of order unity because the assumed $\eta = \eta_0 (T_0/T_e)^{3/2}$ scaling does not take into account that $\ln \Lambda$ depends on temperature.

For Caltech parameters $t_{4\times}=240$ ps which is orders of magnitude shorter than the $\sim 1~\mu s$ duration of the x-ray burst. The catastrophic temperature increase predicted by Eq.16 can be prevented by introducing a power leakage to provide a balance between the energy entering the system and the energy leaving the system. Possible forms of power leakage are atomic line radiation, bremsstrahlung, thermal conductivity, and loss of fast particles at a material surface. Equation 1 shows that the rapid increase in temperature will cause a rapid reduction of E_D so if initially $E < E_D$, unless there is a power leakage, the situation will quickly change to $E > E_D$ even though E is constant. Thus, without a power leakage mechanism, runaway will eventually occur for any finite electric field even if it is extremely small.

VI. DERIVATION OF THE MODEL

Instead of working in the electron center of mass frame which is a non-inertial frame if there is not a steady-state, all calculations are done in the plasma center of mass frame which is an inertial frame even if there is not a steady state. Furthermore, unlike the classical theory, no assumption is made regarding electron or ion velocity distribution functions being Maxwellians, shifted Maxwellians, or Maxwellians plus a perturbation. Instead, these velocity distribution functions are assumed to start as Maxwellians but then are allowed to evolve in a way dictated by the combination of the binary encounters and an applied electric field. The evolution of the individual three-dimensional velocity vectors of a large number N of interacting particles is calculated numerically from all possible binary encounters between N/2 electrons and N/2 ions. This calculation is done first with no electric field to establish an initial condition where electrons and ions have same-temperature Maxwellian velocity distributions. A spatially uniform electric field $\mathbf{E} = E\hat{z}$ is then turned on and the time-dependent evolution of the velocity distributions is calculated numerically. For binary interactions where the relative velocity is less than the electron thermal velocity, the impact parameter ranges from infinitesimal to the electron Debye length. For binary interactions where the relative velocity exceeds the electron thermal velocity, the impact parameters range from infinitesimal to half of the inter-particle distance $L = n^{-1/3}$. Half the inter-particle distance is used as the upper bound for superthermal electrons because field particles cannot move sufficiently fast to establish Debye shielding clouds around superthermal electrons. The interparticle distance is used when there is no Debye shielding because if a test particle is less than the interparticle distance from a given field particle, the forces from all other field particles are in random directions and so cancel. Detailed justification for this is provided in Appendix B. The distinction of whether to use the Debye length or the inter-particle distance as the upper bound turns out to be of negligible importance. This is because if the interparticle distance L is used for the upper bound, then the logarithmic integral $\int db/b$ evaluates to

$$\ln\left(\frac{L}{b_{\pi/2}}\right) = \ln\left(4\pi \left(n\lambda_D^3\right)^{2/3}\right). \tag{19}$$

Thus, for $n\lambda_D^3 \gg 1$ the ratio of the two types of logarithms is

$$\frac{\ln\left(4\pi\left(n\lambda_D^3\right)^{2/3}\right)}{\ln\left(4\pi n\lambda_D^3\right)} = \frac{\ln 4\pi + \frac{2}{3}\ln\left(n\lambda_D^3\right)}{\ln 4\pi + \ln\left(n\lambda_D^3\right)} \simeq \frac{2}{3}$$
(20)

where the approximation is made because $n\lambda_D^3 \gg 1$.

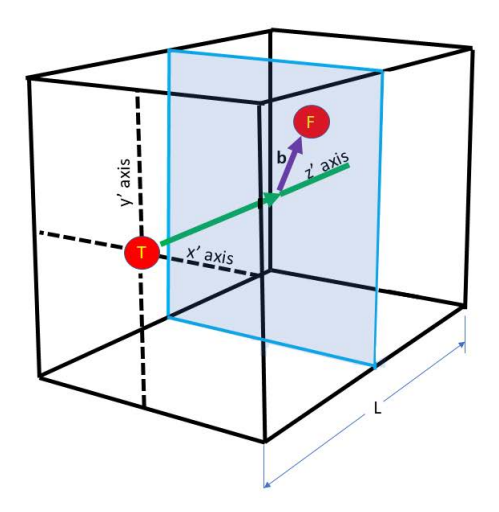


FIG. 2. Scattering cube with side dimension $L = n^{-1/3}$ contains one field particle 'F' at a random position $\bf b$ in the blue-shaded x'y' plane which is at a random position z'. The impact parameter is thus $\bf b$. The z' axis is defined by the direction of the initial relative velocity. The test particle 'T' will experience a binary encounter with the field particle if $z' < v_{rel}\Delta t$. The scattering is calculated in the center of mass frame of the test and field particles and then transformed back to the lab frame. The green arrow describes the trajectory the test particle T would make if there were no field particle.

To set up the numerical method, the plasma volume is conceptually subdivided into cubes having side dimension equal to the inter-particle spacing distance $L = n^{-1/3}$ and the change in velocity of all particles is calculated for successive time increments Δt . The orientation of each cube depends on the binary encounter occurring in the cube. A typical cube is sketched in Fig.2. There is a single field particle F at a random location inside the cube so a test particle T could have a binary encounter with this field particle F when the test particle T is in the cube. As sketched in Fig.2, each cube has a local Cartesian coordinate system $\{x',y',z'\}$ with origin defined to be where the test particle enters the cube. The cube orientation is such that the cube z' axis is parallel to the incident relative velocity of the test particle with respect to the field particle. The collision occurs in an x'y' plane located at some position z'; this plane is shaded blue in Fig.2. The field particle is assumed to be at a random location in this x'y' plane so (i) the scattering is in a random direction perpendicular to the z' axis and (ii) the impact parameter magnitude b can have any value up to $L/\sqrt{2}$ if the velocity of the encounter exceeds the thermal velocity (no Debye shielding) and up to λ_{De} if the velocity of the encounter is less than the thermal velocity (Debye shielding operative). Binary encounters can be electron-electron, electron-ion, or ion-ion. The term binary

encounter is used rather than collision as collision has the implication of a $\pi/2$ deflection whereas the deflection resulting from a binary encounter could be any angle $0 < \theta \le \pi$.

Consider a test particle T having a binary encounter with a field particle F in the presence of a uniform, constant background electric field $\mathbf{E} = E_z \hat{z}$. The test and field particle equations of motion are

$$\frac{d\mathbf{v}_T}{dt} = \frac{q_T q_F}{4\pi\varepsilon_0 m_T r^3} \mathbf{r} + \frac{q_T}{m_T} E_z \hat{z}$$
 (21a)

$$\frac{d\mathbf{v}_F}{dt} = -\frac{q_T q_F}{4\pi\varepsilon_0 m_F r^3} \mathbf{r} + \frac{q_F}{m_F} E_z \hat{z}.$$
 (21b)

where

$$\mathbf{r} = \mathbf{r}_T - \mathbf{r}_F. \tag{22}$$

The relative velocity is

$$\mathbf{v} = \mathbf{v}_T - \mathbf{v}_F \tag{23}$$

and the center of mass velocity is

$$\mathbf{V} = \frac{m_T \mathbf{v}_T + m_F \mathbf{v}_F}{m_T + m_F} \tag{24}$$

with the inverse relations

$$\mathbf{v}_T = \mathbf{V} + \frac{\mu}{m_T} \mathbf{v} \tag{25}$$

$$\mathbf{v}_F = \mathbf{V} - \frac{\mu}{m_F} \mathbf{v}. \tag{26}$$

The kinetic energy of the two particles can be decomposed into components associated with the center of mass and kinetic energy associated with the relative velocity since

$$\frac{1}{2}m_F v_F^2 + \frac{1}{2}m_T v_T^2 = \frac{1}{2}(m_F + m_T)V^2 + \frac{\mu}{2}v^2.$$
 (27)

We introduce a reference velocity v_0 to avoid assuming the existence of a Maxwellian velocity distribution and its associated well-defined temperature. To make contact with the classical theory, the reference velocity is assumed to be the initial electron thermal velocity, i.e., $v_0 = \sqrt{2\kappa T_e(0)/m_e}$. From Eq.8 the impact parameter for scattering by $\pi/2$ for a reduced mass particle μ moving at the reference velocity v_0 is

$$b_{\pi/2,0} = \frac{e^2}{4\pi\varepsilon_0\mu v_0^2}. (28)$$

We define a Debye-like length

$$\lambda_f = \sqrt{\frac{\varepsilon_0 \mu_e v_0^2}{ne^2}} \tag{29}$$

where

$$\mu_e = \frac{m_e}{2} \tag{30}$$

is the reduced mass for electron-electron collisions. The definition of λ_f introduces a Debyelike length scale without having to assume that Debye shielding is operative. We further define a Coulomb-like parameter

$$\Lambda_f = 4\pi n \lambda_f^3 \tag{31}$$

and, motivated by the Dreicer runaway analysis¹², define a reference electric field

$$E_0 = \frac{ne^3}{8\pi\varepsilon_0^2 \mu_e v_0^2} = \frac{neb_{\pi/2,0}}{2\varepsilon_0} \frac{\mu}{\mu_e}.$$
 (32)

 E_0 is about an order of magnitude smaller than the Dreicer field since E_0 does not contain the $\ln\left(\lambda_D/b_{\pi/2}\right)$ factor in the Dreicer field. Because $\mu_e v_0^2 = \kappa T_e$ it is seen that E_0 is one half the electric field produced by a single electron where the field is measured at a distance λ_{De} from the electron, that is, $E_0 = \frac{1}{2} \frac{e}{4\pi\epsilon_0 \lambda_{De}^2}$.

Defining the drift velocity

$$\mathbf{u}_d = \mathbf{u}_i - \mathbf{u}_e \tag{33}$$

so $\mathbf{J} = ne\mathbf{u}_d$, defining the normalized electric field as $\mathbf{\bar{E}} = \mathbf{E}/E_0$, and defining the normalized drift velocity as $\mathbf{\bar{u}}_d = \mathbf{u}_d/v_0$, then Ohm's law, Eq.13, becomes

$$\bar{\mathbf{E}} = \frac{4\ln\Lambda}{3\sqrt{\pi}}\,\bar{\mathbf{u}}_d. \tag{34}$$

We define a reference time

$$\tau = \frac{b_{\pi/2,0}}{v_0} \tag{35}$$

so $\tau/v_0=b_{\pi/2,0}/v_0^2$ has units of inverse acceleration.

The Caltech experiment will be used as a tangible example. The Caltech experiment had $n=10^{22}~\text{m}^{-3}$, T=2~eV, and the transient electric field associated with x-ray production is 60 kV/m. The reference velocity is $v_0=\sqrt{2\kappa T_e/m_e}=8\times10^5~\text{m/s}$, $E_0=70~\text{kV/m}$, $\lambda_f=10^{-7}~\text{m}$, and $\Lambda_f=146$ (see Table II).

The first and second terms on the right hand sides of Eqs. 21a and of Eq.21b will be respectively called the Coulomb and macroscopic electric field accelerations. Each of these terms individually conserves total particle momentum.

We normalize time to τ , lengths to $b_{\pi/2,0}$, velocity to v_0 , electric field to E_0 and denote normalized quantities by a bar. On multiplying Eqs. 21a and Eq.21b by τ/v_0 , we obtain the normalized equations

$$\frac{d\bar{\mathbf{v}}_T}{d\bar{t}} = \frac{\mu}{m_T} \left(s \frac{\bar{\mathbf{r}}}{\bar{r}^3} + \frac{q_T}{e} \frac{\mu_e^2}{\mu^2} \frac{\bar{E}_z}{2\Lambda_f^2} \hat{z} \right)$$
(36a)

$$\frac{d\bar{\mathbf{v}}_F}{d\bar{t}} = \frac{\mu}{m_F} \left(-s \frac{\bar{\mathbf{r}}}{\bar{r}^3} + \frac{q_F}{e} \frac{\mu_e^2}{\mu^2} \frac{\bar{E}_z}{2\Lambda_f^2} \hat{z} \right)$$
(36b)

where s = +1 if $q_T q_F$ is positive and s = -1 if $q_T q_F$ is negative.

Subtracting Eq. 36b field from Eq.36a gives

$$\frac{d\bar{\mathbf{v}}}{d\bar{t}} = s\frac{\bar{\mathbf{r}}}{\bar{r}^3} + F\hat{z} \tag{37}$$

where

$$F = \left(\frac{\mu}{m_T} \frac{q_T}{e} - \frac{\mu}{m_F} \frac{q_F}{e}\right) \frac{\mu_e^2}{\mu^2} \frac{\bar{E}_z}{2\Lambda_f^2}.$$
 (38)

We note that Eq.37 is called the Stark problem and that analytic solutions have been published (e.g., see Lantoine and Russell³⁰). However, these analytic solutions are exceedingly complex and because F is very small, a much simpler approximate method suffices. It is seen that

$$F = \begin{cases} 0 \text{ for like-particle binary encounters (ion-ion, electron-electron binary encounters)} \\ \frac{q_T}{e} \frac{\mu_e^2}{\mu^2} \frac{\bar{E}_z}{2\Lambda_f^2} \text{ for unlike-particle binary encounters (electron-ion, ion-electron binary encounters)}. \end{cases}$$
(39)

Adding m_T times Eq. 36a to m_F times Eq. 36b gives

$$(m_T + m_F) \frac{d\bar{\mathbf{V}}}{d\bar{t}} = \mu \left(\frac{q_T}{e} + \frac{q_F}{e}\right) \frac{\mu_e^2}{\mu^2} \frac{\bar{E}_z}{2\Lambda_f^2} \hat{z}$$
(40)

so

$$\frac{d\bar{\mathbf{V}}}{d\bar{t}} = \begin{cases}
\frac{q_T}{2e} \frac{\mu_e^2}{\mu^2} \frac{\bar{E}_z}{2\Lambda_f^2} \hat{z} & \text{ for like-particle binary encounters (ion-ion, electron-electron binary encounters)} \\
0 & \text{ for unlike-particle binary encounters (electron-ion, ion-electron binary encounters)}.
\end{cases}$$
(41)

Equations 36a and 36b show that two plasmas having the same \bar{E}_z and the same Λ_f behave similarly and, in general, $\bar{E}_z/\Lambda_f^2 \ll 1$. For the Caltech jet parameters $\bar{E}_z/2\Lambda_f^2 = 2.2 \times 10^{-5}$.

We restrict consideration to situations where the electric field is sub-Dreicer and so consider only $\bar{E}_z < 1$ since the behavior of a super-Dreicer electric field is known. The effect of the sub-Dreicer electric field when the particle traverses a cube is thus small so the electric field does not appreciably change the particle trajectory. This implies that the Coulomb collision and the macroscopic electric field can be considered to be independent, additive effects.

The electric field accelerates electrons and ions in opposite z directions and so tends to make a z-directed electric current. On the other hand, binary encounters tend to (i) attenuate this electric current, (ii) isotropize the distribution functions, and (iii) equipartition energy between electrons and ions so that electrons and ions develop the same temperature. Because power is being injected, the system becomes hotter as time progresses as outlined in Eq.15. This contrasts with the classical theory where the system is assumed to have a steady-state temperature despite being heated by Ohmic dissipation (e.g., see Kulsrud $et\ al.\ ^{13}$).

Depending on whether s=1 or s=-1 in Eq.37, θ will be positive or negative. However, the direction of $\bar{\bf b}$ also affects whether θ is positive or negative. Because $\bar{\bf b}$ has equal probability of being in the positive or negative y' direction, there is equal probability of scattering in the positive or negative θ directions for each of the s=+1 and s=-1 situations. Thus, the \pm sign for θ is automatically taken into account by having random orientations of $\bar{\bf b}$ and so from now on s=1 will be assumed.

Since lengths are normalized to $b_{\pi/2,0}$ which was prescribed by Eq.28, the normalized interparticle spacing is

$$\bar{L} = (4\pi)^{1/3} \frac{\mu}{\mu_e} \Lambda_F^{2/3}.$$
 (42)

The length of a side of a normalized cube containing one nominal field particle is thus \bar{L} . The normalized electron Debye length is

$$\bar{\lambda}_{De} = \frac{\mu}{\mu_e} \Lambda_f. \tag{43}$$

The range of the normalized impact parameter \bar{b} is thus

$$0 < \bar{b} < \frac{1}{2}\bar{L}$$
 for superthermal particles (44)

$$0 < \bar{b} < \bar{\lambda}_{De}$$
 for subthermal particles. (45)

The new relative velocity $\bar{\mathbf{v}}^{new}$ is given by the Rutherford scattering formula Eq.8 as

$$\bar{\mathbf{v}}^{new} = \bar{\mathbf{v}}\cos\theta + \frac{\bar{\mathbf{b}}}{|\bar{\mathbf{b}}|} |\bar{\mathbf{v}}| \sin\theta \tag{46}$$

where $\bar{\mathbf{b}}$ is a randomly directed vector in the x'y' plane starting from x' = 0, y' = 0 at some z' position where $0 < z' < \bar{L}$. Thus, the scattering is a rotation of $\bar{\mathbf{v}}$ by an angle θ about the x' axis.

We define

$$\delta = \frac{1}{\bar{b}\bar{v}^2} \tag{47}$$

where $0 < \delta < \infty$. Equation 8 can thus be expressed as

$$\tan(\theta/2) = \delta \tag{48}$$

where

$$\cos \theta = \frac{1 - \delta^2}{1 + \delta^2} \tag{49}$$

$$\sin \theta = \frac{2\delta}{1 + \delta^2}.\tag{50}$$

These show that $\theta = \pi$ when $\delta \to \infty$, that $\theta = \pi/2$ when $\delta = 1$ and that $\theta \to 2\delta$ when $\delta \ll 1$. The definition of δ and the form of Eqs. 49 and 50 are the same as used in Eq.7 of Takizuka and Abe ¹⁴.

Equation 37 is solved numerically as follows:

1. A suitable time step $\Delta \bar{t}$ is defined in a manner that relates to item 5 in Sec.IV but is more precise because the definition here takes into account that a particle is in fact scattered after each binary encounter whereas item 5 in Sec.IV does not take this scattering into account. The goal is to take into account that faster particles make more collisions per time. Here, this is allowed for by considering what happens inside a single scattering cube rather than averaging over many scattering cubes. This is done by noting that a field particle could be located anywhere inside a scattering cube so a very slow test particle might not reach a field particle if the field particle is at the far end of the scattering cube and the assumed time step is very short.

Specifically we choose $\Delta \bar{t}$ to be the time for a superthermal particle with normalized velocity β to travel the cube length \bar{L} . This defines the time step $\Delta \bar{t}$ to be used for all particles as

$$\Delta \bar{t} = \frac{\bar{L}}{\beta}.\tag{51}$$

The normalized time-steps $\Delta \bar{t}$ for ion-ion, electron-electron, and electron-ion encounters differ because \bar{L} differs, but the un-normalized time step is the same for ion-ion, electron-electron, and electron-ion encounters since the un-normalized time step is

$$\Delta t = \frac{\bar{L}}{\beta} \tau = \frac{\bar{L}}{\beta} \frac{b_{\pi/2,0}}{v_0} = \frac{1}{\beta} \frac{n^{-1/3}}{v_0}.$$
 (52)

Choosing $\beta=10$ and using the Caltech parameters $(n^{-1/3}=4.6\times 10^{-8} \text{ m}, \ v_0=8.4\times 10^5 \text{ m/s})$ gives an un-normalized time step $\Delta t=5.5\times 10^{-15} \text{ s}$. Since 4 ns is required to accelerate an electron to 6 keV, following the complete acceleration would require 10^6 time steps. Such a large number of time steps is impractical since $\sim 10^8$ interactions are calculated for each time step. Instead, a smaller number of time steps will be used to examine the initial evolution of the distribution function. The value $\beta=10$ is chosen as a compromise because if a very large β is chosen, then thermal and subthermal particles could only travel an infinitesimal distance into the cube during $\Delta \bar{t}$ and so would have negligible chance of colliding with another particle. Thus $\beta=10$ allows resolving what happens to particles ranging from subthermal to ten times thermal velocity during the time $\Delta \bar{t}$ that they are in a scattering cube.

2. The types of scattering can be decomposed into weak scattering (large impact parameter, small deflection, cumulative effect dominates) and strong scattering (small impact parameter, large deflection, so infrequent as to be relatively unimportant). The normalized electric field is very small (Table II shows that $\bar{E}_z/2\Lambda_f^2=2\times 10^{-5}$) and so for both weak and strong scattering the electric field will make a small perturbation to the test particle trajectory. Since this perturbation is small, it will be linear in the strength of the electric field. However, for the Coulomb force, there is a difference between the weak and strong scattering cases. In the weak scattering case, the perturbation to the trajectory is small and so is also linear in the strength of the Coulomb force. In this case, the effects of the electric field and the Coulomb force can simply be added in any order since both are linear. However, in the case of strong scattering, the particle trajectory is substantially altered by the Coulomb force and so the change in trajectory is not a small perturbation. As an extreme example, the Coulomb force might reverse the direction of a particle initially moving in the z direction. If the electric field is also in the z direction, then the electric field would accelerate the particle before the encounter and then decelerate the particle after (or vice versa depending on the signs). To encompass this possibility, the particle motion is decomposed into the

interval before Coulomb scattering, the Coulomb scattering, and the interval after Coulomb scattering. Thus, there would be electric field acceleration during an interval $\Delta t/2$ before Coulomb scattering and then additional electric field acceleration during an interval $\Delta t/2$ after Coulomb scattering. This characterization will then encompass both weak and strong scattering; the time decomposition does not matter for weak scattering but is important for strong scattering.

However, as will be discussed below, it is also possible that during the entire Δt there is no Coulomb scattering and only electric field acceleration. Integration of Eq.37 for the pre-Coulomb interval gives

$$\bar{\mathbf{v}}(t + \Delta t/2 - \varepsilon) = \bar{\mathbf{v}}(t) + \mathbf{F}\Delta t/2 \tag{53}$$

where ε represents an infinitesimal time interval. The Coulomb scattering, if it occurs, is calculated using $\bar{\mathbf{v}}(t + \Delta t/2 - \varepsilon)$ as the incident velocity. This gives

$$\cos \theta^* = \frac{1 - (\delta^*)^2}{1 + (\delta^*)^2} \tag{54}$$

$$\sin \theta^* = \frac{2\delta^*}{1 + (\delta^*)^2} \tag{55}$$

where

$$\delta^* = \frac{1}{\bar{b} \left[\bar{\mathbf{v}} (t + \Delta t / 2 - \varepsilon) \right]^2}.$$
 (56)

The relative velocity is updated in the event of a Coulomb scattering to be

$$\bar{\mathbf{v}}(t + \Delta t/2 + \varepsilon) = \bar{\mathbf{v}}(t + \Delta t/2 - \varepsilon)\cos\theta^* + \frac{\bar{\mathbf{b}}}{|\bar{\mathbf{b}}|}|\bar{\mathbf{v}}(t + \Delta t/2 - \varepsilon)|\sin\theta^*. \tag{57}$$

The post-Coulomb acceleration is then calculated to give

$$\bar{\mathbf{v}}(t + \Delta t) = \bar{\mathbf{v}}(t + \Delta t/2 + \varepsilon) + \mathbf{F}\Delta t/2. \tag{58}$$

3. The decision on whether or not there is a Coulomb scattering is determined as follows: The field particle F is assumed to have an equal chance of being located anywhere in the cell sketched in Fig.2. We consider a relative velocity $\bar{\mathbf{v}}$ with $|\bar{\mathbf{v}}| < \beta$ and consider motion in the center of mass frame where now there is a reduced-mass fictitious particle making an encounter with a fixed scattering center. The particle spacing in the center of mass frame is the same as in the lab frame so the fictitious particle with $|\bar{\mathbf{v}}| < \beta$ will travel a distance less then \bar{L} in time $\Delta \bar{t}$. Its probability of

having an encounter with the scattering center will be given as $P = |\bar{\mathbf{v}}| \Delta t / \bar{L} = |\bar{\mathbf{v}}| / \beta$. Using $\beta = 10$ corresponds to an un-normalized speed $10v_0$, so a particle with un-normalized speed of $2v_0$ will only traverse 20% of \bar{L} . Because the field particle and hence the fixed scattering center have an equal chance of being located anywhere in the cell, the fictitious reduced-mass particle moving at $2v_0$ has only a 20% chance of encountering the scattering center in time $\Delta \bar{t}$. The encounter will thus only occur for 20% of possible encounters. Taking into account the different probabilities of an encounter for different relative velocities corresponds to list item 5 in Section IV which showed that fast particles make more binary encounters than do slow particles in a time Δt . However, the method used here should be more realistic than the method in list item 5 in Section IV because this list item assumed that the impact parameter is the same for successive binary encounters by the incident particle whereas in reality each successive binary encounter has a different impact parameter. Also, list item 5 did not take into account that the direction of $\bar{\mathbf{v}}$ changes after each binary encounter as list item 5 assumed that the particle always travels in the same direction despite undergoing numerous binary encounters each of which is assumed to be changing the direction of the particle. Furthermore, list item 5 did not allow for e-e and e-i binary interactions to be interspersed as the calculation of the Coulomb logarithm assumed a large uninterrupted sequence of e-e collisions or a large uninterrupted sequence of e-i collisions.

The probability P that a scattering occurs in Δt is determined using random numbers. Using a numerically generated random number ρ where $0 < \rho < 1$, the quantity

$$\Upsilon = P - \rho \tag{59}$$

is calculated. If $\Upsilon \geq 0$ the binary encounter calculation proceeds, whereas if $\Upsilon < 0$ it is skipped. For example, the particle moving at $\beta = 10$ will have $\Upsilon > 0$ for all ρ and so its scattering will be calculated for all potential encounters, but a slower particle will have its scattering calculated only for a proportionately smaller fraction of encounters.

The numerical calculation determines updated test and field particle velocities using

$$\mathbf{\bar{v}}_T(t + \Delta t) = \mathbf{\bar{V}}(t + \Delta t) + \frac{\mu}{m_T} \mathbf{\bar{v}}(t + \Delta t)$$
(60)

$$\bar{\mathbf{v}}_F(t+\Delta t) = \bar{\mathbf{V}}(t+\Delta t) - \frac{\mu}{m_F}\bar{\mathbf{v}}(t+\Delta t)$$
(61)

where $\bar{\mathbf{v}}(t + \Delta t)$ is the new relative velocity given by Eq.58 and $\bar{\mathbf{V}}(t + \Delta t)$ is the new center of mass velocity obtained by integration of Eq.41.

To calculate $\bar{\mathbf{v}}(t + \Delta t)$ it is necessary to determine the cube orientation and the impact parameter $\bar{\mathbf{b}}$. The z' direction is defined by the incident relative velocity direction so

$$\hat{z}' = \frac{\mathbf{v}}{|\mathbf{v}|}.\tag{62}$$

Thus, there will be a continuous re-definition of \hat{z}' as the relative velocity is in a different direction for each binary encounter. To determine the impact parameter $\bar{\mathbf{b}}$, two orthogonal unit vectors are constructed that are perpendicular to \hat{z}' and to each other. The first of these unit vectors is

$$\hat{y}' = \frac{(\hat{x} + \hat{y} + p\hat{z}) \times \hat{z}'}{|(\hat{x} + \hat{y} + p\hat{z}) \times \hat{z}'|}$$
(63)

where p is normally set to unity, but in the exceptional situation where \hat{z}' happens to be parallel to $\hat{x} + \hat{y} + \hat{z}$, p is set to 2. Thus, \hat{y}' is a unit vector orthogonal to \hat{z}' . To complete the triad,

$$\hat{x}' = \hat{y}' \times \hat{z}'. \tag{64}$$

Because the field particle is in the cube at a random point in the x'y' plane at some arbitrary z', the field particle position is

$$\bar{\mathbf{r}}_F = \bar{\mathbf{r}}_T + ((\rho_1 - 0.5)\hat{x}' + (\rho_2 - 0.5)\hat{y}' + z'\hat{z}')\bar{L}$$
(65)

where $\rho_{1,2}$ are independent random numbers having values between 0 and 1. This gives

$$\bar{\mathbf{r}} = ((\rho_1 - 0.5)\hat{x}' + (\rho_2 - 0.5)\hat{y}' + z'\hat{z}')\bar{L}. \tag{66}$$

Since the test particle incident velocity is at the origin of the x'-y' plane and in the z' direction, the impact parameter is

$$\bar{\mathbf{b}} = (\rho_1 - 0.5)\bar{L}\hat{x}' + (\rho_2 - 0.5)\bar{L}\hat{y}', \tag{67}$$

i.e., anywhere in the x'y' plane shown as blue in Fig. 2. If Debye shielding is operative, then λ_{De} would replace \bar{L} in Eq. 67 but as shown in Eq.20 this makes little difference.

The required initial conditions are the initial velocities of particles, \bar{E} , Λ_f , and m_i/m_e . Each of the N/2 electrons is labeled by the index i where $0 \le i \le N/2 - 1$ and each of the N/2 ions also have indices i, but with N/2 < i < N-1. This scheme allows for the same index i to refer to both electrons and ions.

The matrix in Eq.68 shows the counting procedure for all possible binary encounters of the N particles with each other for the simplified case where N = 8. Here rows are numbered from i = 0

to 7 and columns are numbered from j = 0 to 7. The indices i = 0, 1, 2, 3 refer to electrons which are labeled as e0, e1, e2, and e3 while the indices i = 4, 5, 6, 7 refer to ions which are labeled as i0, i1, i2 and i3. There are three types of binary encounters, namely electron-electron, electron-ion, and ion-ion. For example, e1 - e0 in the matrix denotes a binary encounter between electron #0 and electron #1. Binary encounters between unlike particles are shown in bold in the matrix.

```
\begin{bmatrix} * \\ 0:e1-e0 & * \\ 1:e2-e0 & 7:e2-e1 & * \\ 2:e3-e0 & 8:e3-e1 & 13:e3-e2 & * \\ 3:\mathbf{i0}-\mathbf{e0} & 9:\mathbf{i0}-\mathbf{e1} & 14:\mathbf{i0}-\mathbf{e2} & 18:\mathbf{i0}-\mathbf{e3} & * \\ 4:\mathbf{i1}-\mathbf{e0} & 10:\mathbf{i1}-\mathbf{e1} & 15:\mathbf{i1}-\mathbf{e2} & 19:\mathbf{i1}-\mathbf{e3} & 22:i1-i0 & * \\ 5:\mathbf{i2}-\mathbf{e0} & 11:\mathbf{i2}-\mathbf{e1} & 16:\mathbf{i2}-\mathbf{e2} & 20:\mathbf{i2}-\mathbf{e3} & 23:i2-i0 & 25:i2-i1 & * \\ 6:\mathbf{i3}-\mathbf{e0} & 12:\mathbf{i3}-\mathbf{e1} & 17:\mathbf{i3}-\mathbf{e2} & 21:\mathbf{i3}-\mathbf{e3} & 24:i3-i0 & 26:i3-i1 & 27:i3-i2 & * \end{bmatrix} 
(68)
```

To calculate binary encounters, all elements i,j of the off-diagonal lower half of the matrix are used; the set of all possible binary encounters indexed sequentially is given by the number preceding the colon in the elements in the matrix in Eq.68. For each element i,j a binary encounter is calculated according to Eqs.53 - 61. The procedure described with respect to Eq.59 can now be seen more clearly by considering elements 3-6 in Eq.68 which is a list of all the binary encounters that electron e0 makes with ions. Each element in Eq.68 describes what happens in a time $\Delta \bar{t}$ so the four elements 3-6 describe binary encounters in the time $4\Delta \bar{t}$. If electron e0 has velocity with magnitude β it will collide with all four ions (i.e., with ions i0, i1, i2, i3) in the time $4\Delta \bar{t}$. However, if electron e0 has a velocity with magnitude $\beta/2$ then it only has a chance of having binary encounters with two of these ions. Which ion the electron has an encounter with is random, so Eq.59 is used to determine whether or not the encounter takes place. Thus, only two of the four possible Rutherford scatterings will be calculated. If the electron does not have a Rutherford scattering with an ion during an interval $\Delta \bar{t}$, the electron nevertheless experiences the electric field acceleration.

In order to randomize the calculation, the elements of the Eq.68 matrix are first re-indexed in a linear fashion as shown by the number preceding the colon in each element, e.g. (2:e3-e0) is the linear element 2. This re-indexing is used to construct a 1D vector with $(N^2 - N)/2$ elements

which for this simplified example would be

$$[0:e1-e0, 1:e2-e0, 2:e3-e0, 3:\mathbf{i0}-\mathbf{e0}, \dots 25:i2-i1, 26:i3-i1, 27:i3-i2].$$
(69)

Next, the elements of the vector in Eq.69 are shuffled to produce a 1D vector with $(N^2 - N)/2$ elements having a random order as, for example,

$$[3:\mathbf{i0}-\mathbf{e0}, 24:i3-i0, 4:\mathbf{i1}-\mathbf{e0}, 3:\mathbf{i0}-\mathbf{e0}, \dots 1:e2-e0, 26:i3-i1, 0:e1-e0].$$
(70)

Binary encounters are numerically evaluated in the order of this shuffled vector to avoid patterns that might develop using the unshuffled vector. If $\bar{E}_z = 0$, this procedure yields a Maxwellian (thermal) distribution after a few sequences of Eq.70.

For the Caltech jet experiment $\bar{E}/2\Lambda_f^2=2.2\times 10^{-5}$ which means that during the time a reference electron spends inside a cube, the fractional change in the z component of its velocity as a result of the electric field is very small. If the particle is an ion, then the change in velocity is even smaller. It is important to note that \hat{z} is a lab-frame unit vector so the electric field is always pointing in the same direction in the lab frame whereas the continuously changing \hat{x}', \hat{y}' and \hat{z}' unit vectors could be pointing in any direction.

VII. ORGANIZATION OF THE NUMERICAL COMPUTATION

Binary encounters between the N particles are calculated by sequencing through the elements of Eq.70 using the values of \bar{E}_z and Λ_f given in Table II. A 'sequence' corresponds to a single pass through the $(N^2 - N)/2$ elements in the matrix in Eq.68. When N is larger than a few hundred and $\bar{E}_z = 0$, the particles become Maxwellian in a few sequences and the total system energy and total system momentum are both conserved. Using N = 1000 for code testing and N = 10,000 for ultimate runs provided convenient run times on a desktop computer; for N = 10,000 a sequence consists of calculating 49,995,000 potential binary encounters. An $m_i/m_e = 16$ mass ratio is used so that the effect of large mass ratio can be identified and yet electron and ion behavior can be distinguished and plotted on the same scale.

The system is first run for four sequences with $\bar{E}_z = 0$ to construct electron and ion Maxwellians having zero average velocity; this is labeled as configuration #0. Equipartition between the six degrees of freedom (electron x, y, z motion, ion x, y, z motion) is observed and conservation of total

energy and momentum is also observed. The configuration #0 Maxwellian distributions are stored and used as the initial condition for configurations with finite \bar{E}_z . Further sequences of Eq.70 are then calculated with finite \bar{E}_z and particle velocity distribution functions are constructed from histograms of the velocities. Configurations #1,2,3 have increasing values of $\bar{E}_z/2\Lambda_f^2$ with respective relative scaling proportional to $1, \sqrt{2}, 2$. Configurations #4,5,6 are the same as configuration #2 except that a toy model of atomic line radiation is added to introduce a power leakage. Configurations #1,2,3 show that total particle kinetic energy is no longer conserved when $\bar{E}/2\Lambda_f^2$ is finite, but overall momentum is conserved. To keep the presentation within length limitations, configurations #0, #2, #4, #5, and #6 which contain the essential results will be presented here while configurations #1 and #3 which provide information on dependence on \bar{E}_z are presented in Appendix C with the result summarized here. As predicted by Eq.15, the total particle kinetic energy continuously increases with time if there is no power loss mechanism. After a long time, the rate of increase of electron kinetic energy is m_i/m_e larger than that of ions. Although a steady-state does not exist, the total system momentum is conserved because the electric field imparts equal and opposite momentum changes to electrons and ions. However, in configurations #4,5,6 the system can approach a steady-state as a result of the power leakage assumed for these configurations. The electrons can develop a unidirectional tail with continuously increasing velocity. This system is not in a steady-state although it may be in a quasi-steady state; the electron velocity distribution deviates significantly from Maxwellian and so is more consistent with experimental observations than a Maxwellian would be.

Electron and ion velocity distribution functions $f_{\sigma x}(v)$, $f_{\sigma y}(v)$, and $f_{\sigma z}(v)$ are directly measured from normalized histograms of the numerically evolved velocity components of the N/2 electrons and the N/2 ions. In order to determine the extent to which the velocity distributions are Maxwellian, the mean velocity $\mathbf{u}_{\sigma} = \langle \mathbf{v}_{\sigma} \rangle$ and the mean square velocity $\langle \tilde{\mathbf{v}}_{\sigma}^2 \rangle = \langle (\mathbf{v}_{\sigma} - \mathbf{u}_{\sigma})^2 \rangle$ are calculated for each species from the numerical velocity distribution functions $f_{\sigma j}(v)$. These calculated mean velocities and mean square random velocities are

$$u_{\sigma j} = \int_{-\infty}^{\infty} v f_{\sigma j}(v) dv \tag{71}$$

and

$$\left\langle \tilde{v}_{\sigma j}^{2}\right\rangle = \int_{-\infty}^{\infty} \left(v - u_{\sigma j}\right)^{2} f_{\sigma j}(v) dv.$$
 (72)

These calculated \mathbf{u}_{σ} and $\left\langle \tilde{v}_{\sigma j}^{2}\right\rangle$ are used to construct Gaussian functions for each component

j = x, y, z of each species σ , namely

$$g_{\sigma j}(v_j) = \frac{1}{\sqrt{2\pi \left\langle v_{\sigma j}^2 \right\rangle}} \exp\left(-\frac{\left(v_j - u_{\sigma j}\right)^2}{2\left\langle \tilde{v}_{\sigma j}^2 \right\rangle}\right). \tag{73}$$

Each Gaussian function $g_{\sigma j}(v_j)$ has the properties that

$$u_{\sigma j} = \int_{-\infty}^{\infty} v g_{\sigma j}(v) dv \tag{74}$$

and

$$\langle \tilde{v}_{\sigma j}^2 \rangle = \int_{-\infty}^{\infty} \left(v - u_{\sigma j} \right)^2 g_{\sigma j}(v) dv.$$
 (75)

The system is considered to have reached thermodynamic equilibrium if $f_{\sigma j}(v) \to g_{\sigma j}(v)$; in this case the particles are said to have thermalized. However, being thermalized does not mean that the system is in a steady-state equilibrium as its temperature and its ion-electron relative drift velocity \mathbf{u}_d could be continuously increasing with time. Comparing the histogram of particle velocities to g indicates whether the system has developed a shifted Maxwellian (histogram coincident with g), a Maxwellian plus perturbation, or something else.

VIII. NUMERICAL RESULTS

The numerically calculated time-dependent velocity distribution functions are presented in animations and as plots of the time dependence of energy, momenta, and velocity.

Configuration #0: This configuration produces the thermalization of opposing beams with no macroscopic electric field and no radiative loss. The prescribed initial electron distribution has $\bar{\mathbf{v}} = -\bar{v}_{e0}\hat{z}$ for half the electrons and $\bar{\mathbf{v}} = +\bar{v}_{e0}\hat{z}$ for the other half. For ions, the initial velocities are similarly prescribed as opposing beams with velocities $\bar{\mathbf{v}} = \pm \bar{v}_{i0}\hat{z}$. The initial velocities $\bar{v}_{e0}, \bar{v}_{i0}$ are prescribed to have unit total kinetic energy per electron-ion pair and an ion initial kinetic energy that is twice the electron initial kinetic energy. The reason for this unequal initial prescription is to enable verification that the numerical calculation produces energy equipartition between the electrons and ions. Specifically $\bar{v}_{e0} = \sqrt{2/3}$ and $\bar{v}_{i0} = (2\sqrt{3})^{-1}$ so the initial kinetic energy of an ion-electron pair is $\frac{1}{2}m_ev_{e0}^2 + \frac{1}{2}m_iv_{i0}^2 = 1$ and the initial kinetic energy ratio is $(\frac{1}{2}m_iv_{i0}^2)/(\frac{1}{2}m_ev_{e0}^2) = 2$. Thus, the initial system has zero total momentum and velocity distributions $f_{\sigma}(\bar{\mathbf{v}}) = (N/2)(\delta(\bar{v}_x)\delta(\bar{v}_y)\delta(\bar{v}_z - \bar{v}_{\sigma 0}) + \delta(\bar{v}_x)\delta(\bar{v}_y)\delta(\bar{v}_z + \bar{v}_{\sigma 0}))$. Thermalization is observed to have three time scales: electron-electron (fast) resulting in thermalized electrons,

ion-ion (medium) resulting in thermalized ions, electron-ion (slow) resulting in equipartition of energy between electrons and ions. The result is thermalized electrons and thermalized ions at the same temperature. Figure 3(Multimedia view) is an animation showing the evolution of the configuration #0 electron and ion distribution functions; the still image is the last image of the animation and so shows the thermalized distributions. In Figs.3(a)-(f) (Multimedia view) the solid blue lines are histograms of the numerically calculated particle velocities while the dashed red lines are Maxwellians (Eq.73) having the same energy and mean velocity. The animation shows the time progression – the dashed red lines denoting g from Eq.73 initially deviate from the solid blue lines denoting f and then later overlay the f_{σ} lines. Figure 4(b) shows the somewhat complex evolution of the various quantities: at t = 0, the ion z kinetic energy is, as prescribed, twice that of the electron z kinetic energy and both ion and electron x kinetic energies are zero. It is seen that the electron kinetic energy in the z direction first decreases and then increases. This is because as shown in Figure 4(b) the electrons thermalize first, then the ions, and then there is equipartition of energy between electrons and ions. At $t \simeq 3$ ps, the electron x and z kinetic energies equalize so the electron z kinetic energy decreases while the electron x kinetic energy increases; the electron y kinetic energy (not shown) behaves the same as the x kinetic energy. This equipartitioning of the three components of the electron kinetic energy at 3 ps means that the z component of the electron kinetic energy drops to one third of its initial value at 3ps. By contrast, at $t \simeq 3$ ps. the ion kinetic energies have only slightly changed from their initial value. After 3 ps the electrons slowly receive energy from the ions so all components of the electron kinetic energy slowly increase. On a slower time scale the z and the x components of the ions equalize. By 200 ps there is equipartition of kinetic energy between all directions of electrons and ions. This state at the end of the evolution of configuration #0 serves as the starting point for configurations #1-#6.

Configurations #1-#3: These configurations start with the thermalized particles produced in configuration #0 but now have finite \bar{E}_z . There is no radiation for these configurations. The results of configuration #2 are shown in Figs.5 (Multimedia view) and 6. The results from configurations #1 and #3 are shown in Appendix C and differ in that \bar{E}_z in configuration #1 is $\sqrt{2}$ times smaller than in configuration #2 and \bar{E}_z in configuration #3 is $\sqrt{2}$ times larger; these provide information on the scaling with \bar{E}_z and show that this scaling is consistent with the prediction of Eq. 16. Figure 6 demonstrates that, contrary to the conventional model, a steady-state does not result in a collisional plasma having a uniform, constant electric field and no other effects. The time for the total kinetic energy to quadruple as seen in Fig. 6(a) is approximately 100 ps which is the same order of

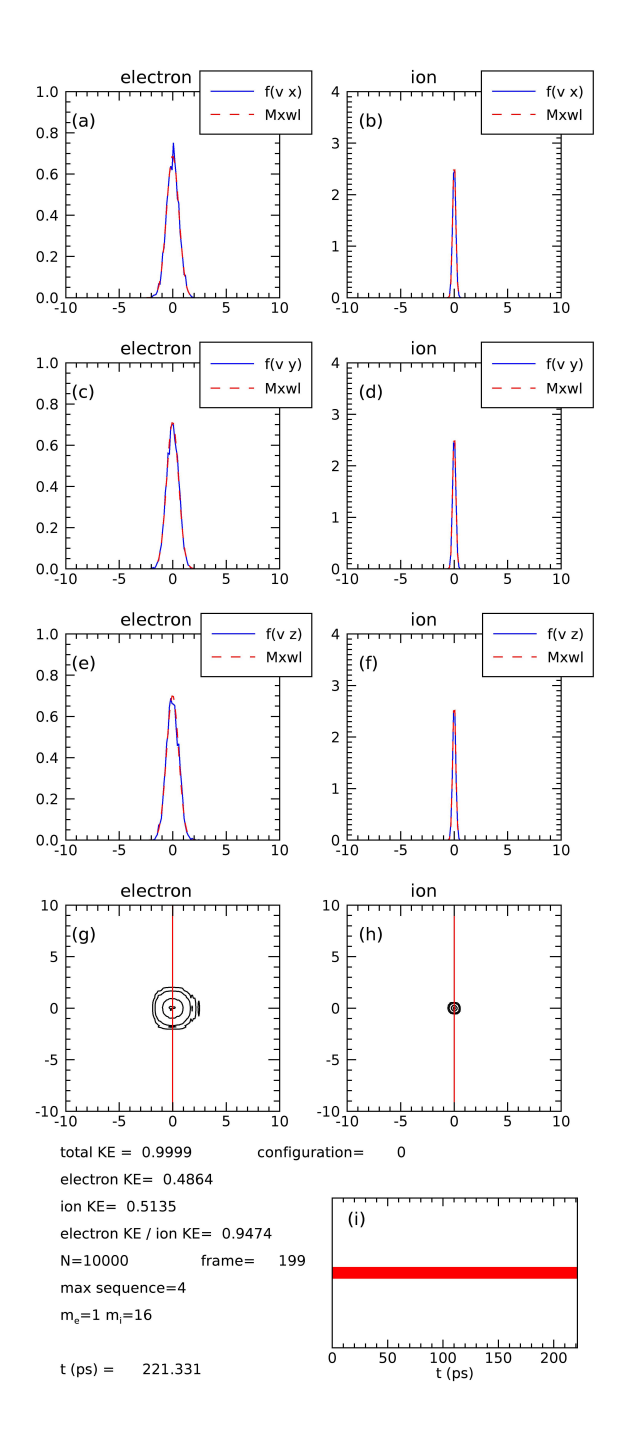


FIG. 3. Initial thermalization starting with distribution functions $f_{\sigma}(\bar{\mathbf{v}}) \sim \delta(\bar{v}_x)\delta(\bar{v}_y)\delta(\bar{v}_z - \bar{v}_{\sigma 0}) + \delta(\bar{v}_x)\delta(\bar{v}_y)\delta(\bar{v}_z + \bar{v}_{\sigma 0})$ and no electric field, no radiation. Blue lines in (a)-(f) are components of electron and ion velocity distributions. (g),(h) are contour plots of electron and ion velocity distributions with horizontal axis being z direction, vertical axis being perpendicular to z. (i) is clock for animation running time. Red dashed lines in (a)-(f) are Maxwellians with same energy and mean velocity. First 10 frames of animation run slowly to provide temporal resolution of rapid electron thermalization. Still image in print version is last frame of animation. (Multimedia view)

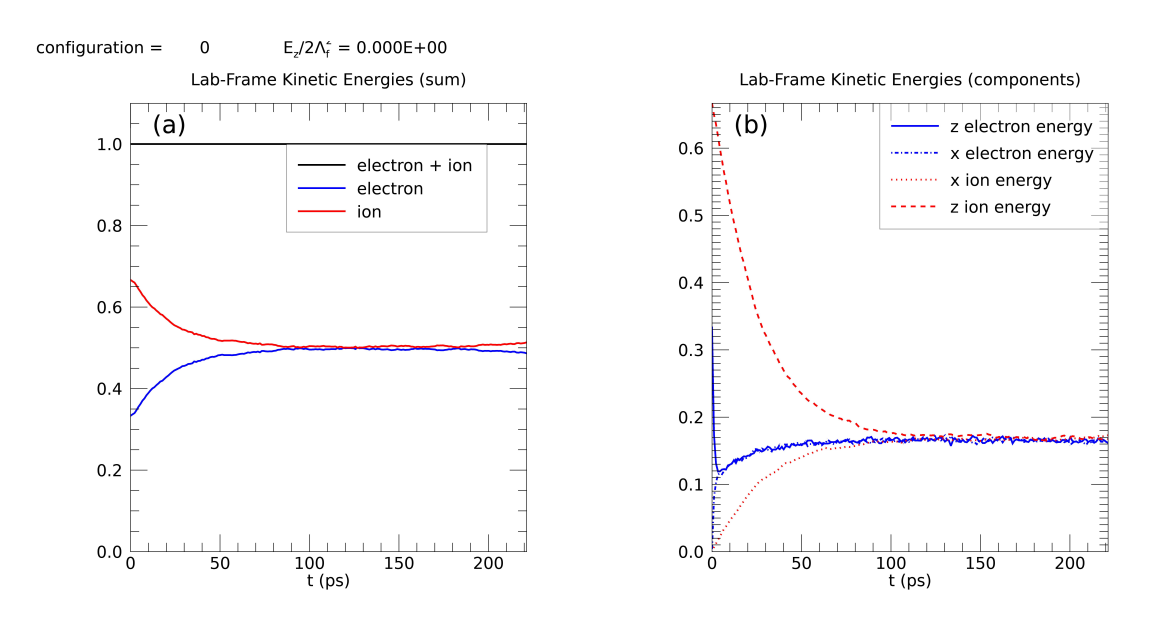


FIG. 4. (a) Time evolution of total kinetic energy of ions, of electrons, and of sum of electrons and ions, (b) time evolution of kinetic energy of z and x components (y component same as x from symmetry).

magnitude as the 240 ps estimate in Eq. 16; the reason for the discrepancy in these quadrupling times is discussed in Sec.VIII A. The respective quadrupling times for configurations #1 and # 3 are respectively a factor of two slower and faster than that of configuration #2 consistent with the $t_{4x} \sim 1/\bar{E}_z^2$ scaling predicted by Eq. 16. The salient feature is the continuous electron acceleration in the negative z direction. This continuous acceleration is not predicted by the classical Fokker-Planck model for a sub-Dreicer electric field.

Configurations #4-#6: These configurations are the same as configuration #2 except that now, in addition, a toy model radiative power loss mechanism has been added. This toy model modifies selected electron-ion binary encounters when the relative kinetic energy exceeds a prescribed threshold corresponding to the energy required to excite an ion from its initial quantum energy state to a higher energy state. If this excitation occurs, then the electron-ion collision is inelastic as there must be a conversion of electron kinetic energy into ion excitation energy. The excited ion emits a photon containing energy corresponding to the difference between the higher and lower quantum energy states. Not all binary encounters with relative kinetic energy exceeding the threshold result in this excitation and associated photon emission because, for the ion excitation to occur, the electron must be physically close to the ion; an extreme grazing collision with the requisite relative kinetic energy would not cause ion excitation because the electron and ion are

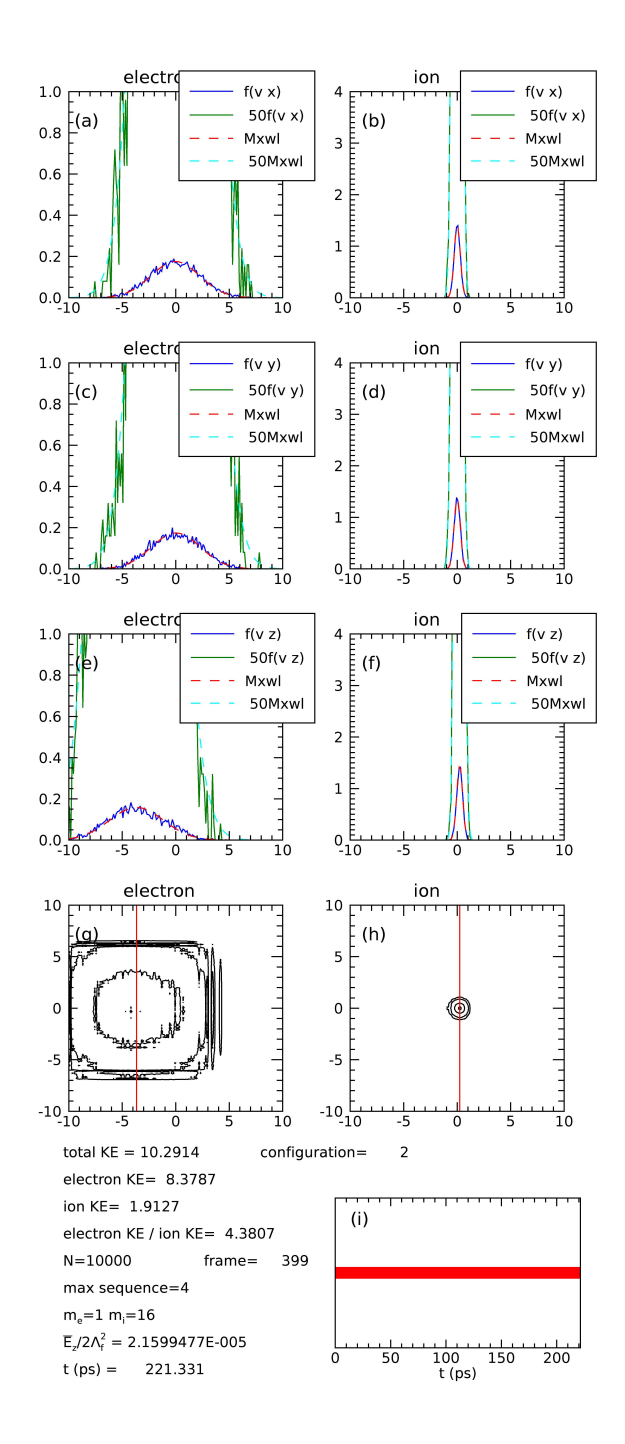


FIG. 5. Configuration #2. (still figure is last figure of animation). $\bar{E}_z/2\Lambda_f^2=2.16\times 10^{-5}$ and no radiation. (a)-(f) show as blue lines the components of numerically computed velocity distribution function f. Also shown (red dashed lines) is the Maxwellian g defined by Eq.73 having same average kinetic energy and same mean velocity. Also shown (dark green and dashed light green) are plots of 50f and 50 g. Contours in (g) and (h) are at 0.001, 0.01, 0.25 and 0.9. Red vertical line in (g) and (h) denote mean z velocity, i.e., $u_{\sigma z}$. (i) is clock for animation running time. (Multimedia view)

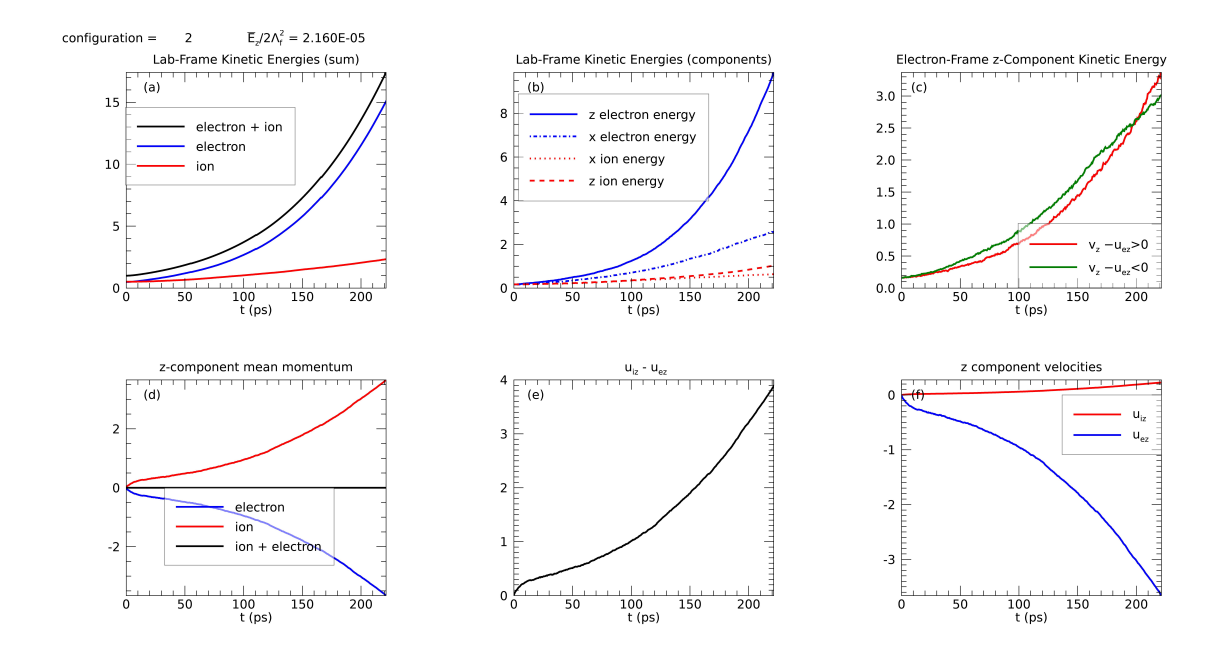


FIG. 6. Configuration #2. (a) Lab-frame kinetic energies for sum of all direction components, (b) lab-frame kinetic energy of z and x components (y same as x), (c) electron-frame kinetic energy z components in positive and negative directions (note that these are not equal contrary to assumption in Eq.A.6 and also no equilibrium is achieved), (d) shows that momentum is conserved, (e) shows that $u_{i,z} - u_{e,z}$ increases without bound (i.e., current density increases without bound), (f) shows that $u_{i,z}$ and $u_{e,z}$ increase without bound.

too far apart.

The photon emission provides a power loss mechanism and so provides the possibility for a steady state to develop. The fact that only a fraction of energetic electrons having the requisite energy make inelastic binary encounters corresponds to this process having an effective cross-section. The numerical representation for this inelastic collision mechanism is that an electron colliding with a relative velocity exceeding $\bar{v}_{crit} = 2$ and with parameter $\delta > \delta_{crit}$ defined by Eq.56 will have its kinetic energy reduced by $m_e \bar{v}_{crit}^2/2$. Since here the energy is normalized such that $\bar{v} = 1$ corresponds to 2 eV electron kinetic energy, then $\bar{v}_{crit} = 2$ corresponds to an electron having four times as much energy, that is 8 eV. Thus, the numerical representation for the inelastic collision is that an electron with energy exceeding 8 eV having a binary encounter with an ion will lose 8 eV providing the encounter is such that $\delta > \delta_{crit}$. After the inelastic collision, the electron proceeds in the same direction as before but, to account for the energy loss, its velocity is reduced such that $\bar{v}^2 \to \bar{v}^2 - \bar{v}_{crit}^2$. A corresponding loss of electron momentum is calculated and the ion momentum is increased by this amount to maintain conservation of momentum. The

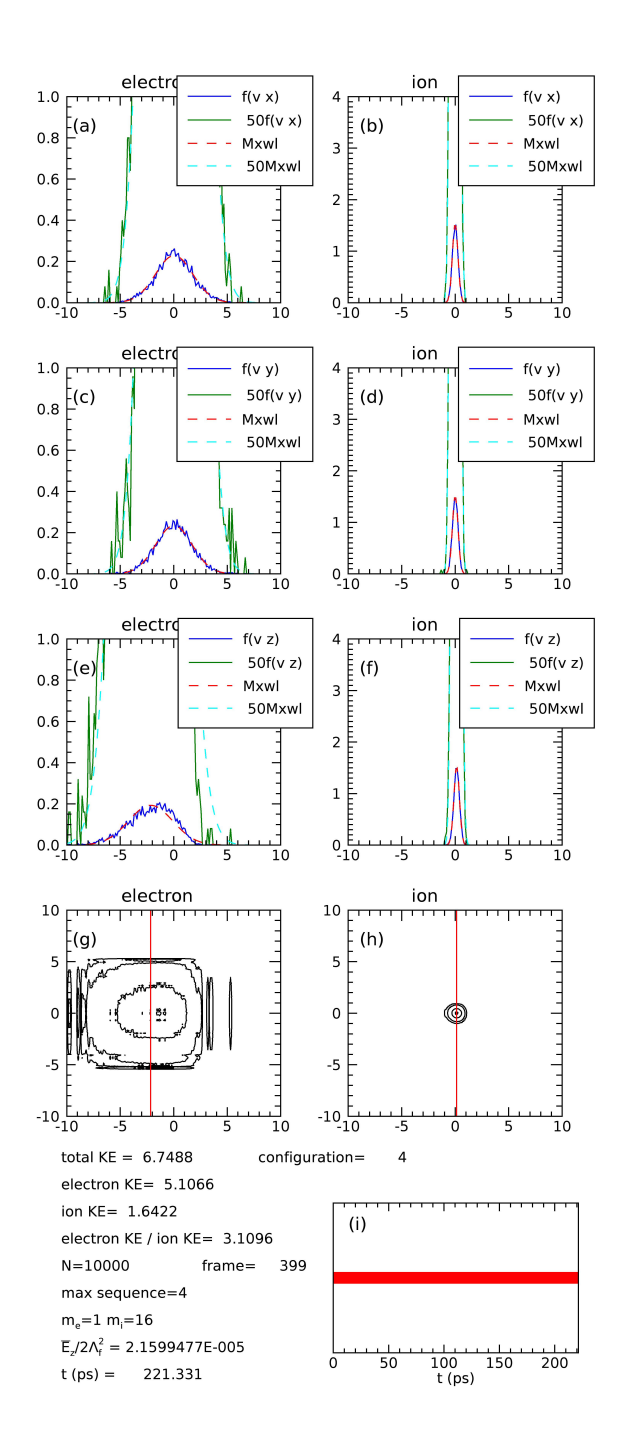


FIG. 7. Configuration #4. (still figure is last figure of animation). Electric field same as Configuration #2 shown in Fig.5 but now the calculation includes a toy model with inelastic binary encounter for electrons with relative velocity exceeding $v_{crit}^- = 2$ and $\delta > \delta_{crit}$ where $\delta_{crit} = 0.3$. This inelastic binary encounter models an electron exciting an ion to a higher energy state and the ion then emitting a photon containing the energy transferred from the electron during the encounter. (Multimedia view)

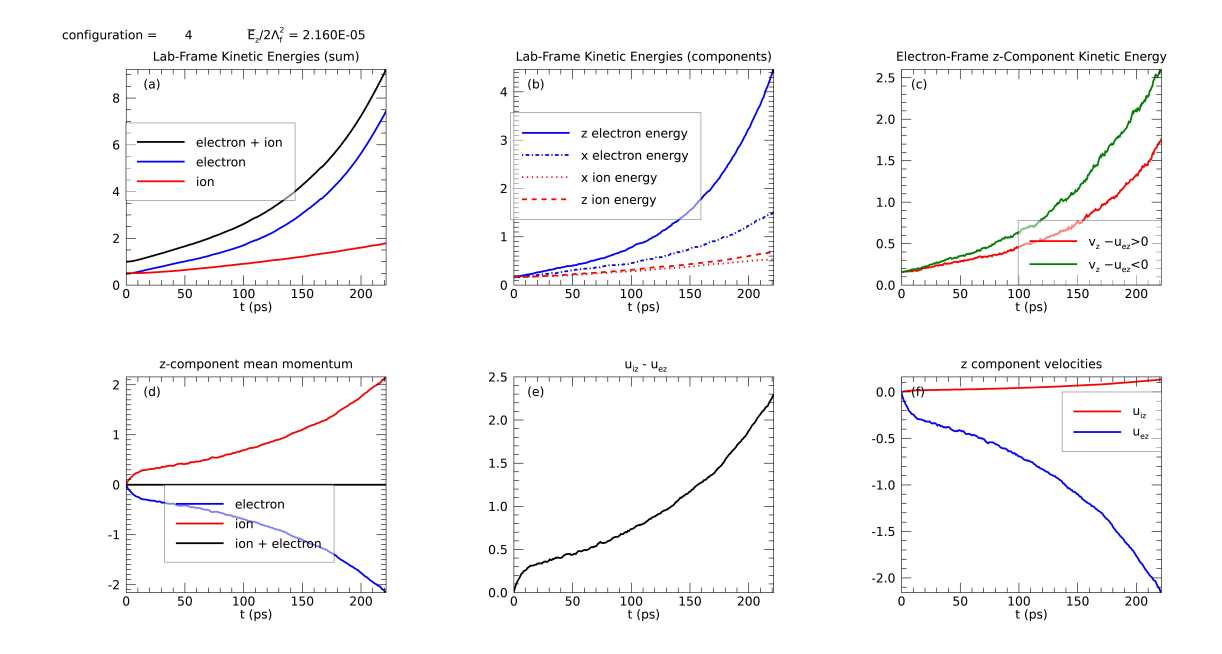


FIG. 8. Configuration #4. Electric field same as Configuration #2 but now calculation includes toy model with inelastic binary encounter for electrons with velocity exceeding $v_{crit} = 2$ and $\delta > \delta_{crit}$ where $\delta_{crit} = 0.3$. This inelastic binary encounter models an electron exciting an ion to a higher energy state and the ion then emitting a photon containing the energy transferred from the electron during the encounter.

 $\delta > \delta_{crit}$ threshold can be expressed in terms of a critical impact parameter \bar{b}_{crit} since Eqs. 28 and 47 imply

$$\delta_{crit} = \frac{1}{b_{crit}} \frac{e^2}{4\pi \varepsilon_0 m_e v^2}.$$
 (76)

SO

$$b_{crit} = \frac{e^2}{4\pi\varepsilon_0 m_e v^2 \delta_{crit}}. (77)$$

This gives an effective inelastic collision cross-section which can be evaluated to be

$$\sigma_{inelastic} = \pi b_{crit}^2 = \pi \left(\frac{e^2}{4\pi \varepsilon_0 m_e \left(\bar{v}_{crit} v_0 \right)^2 \delta_{crit}} \right)^2. \tag{78}$$

Configuration #4 uses $\delta_{crit} = 0.3$ for which Eq.78 gives $\sigma = 2.8 \times 10^{-19}$ m². Configuration #5 has $\delta_{crit} = 0.1$ giving $\sigma = 2.5 \times 10^{-18}$ m² and configuration #6 has $\delta_{crit} = 0.03$ giving $\sigma = 2.8 \times 10^{-17}$ m². Thus, the toy model excitation cross-section is about two to three orders of magnitude larger than actual electron-ion excitation cross sections (e.g., see Fig. 7 of Boffard et al.³¹) and so provides a qualitative representation of reality. Choosing large δ_{crit} requires a more head-on collision and so is more realistic, but this decreases the frequency of occurrence so that many more

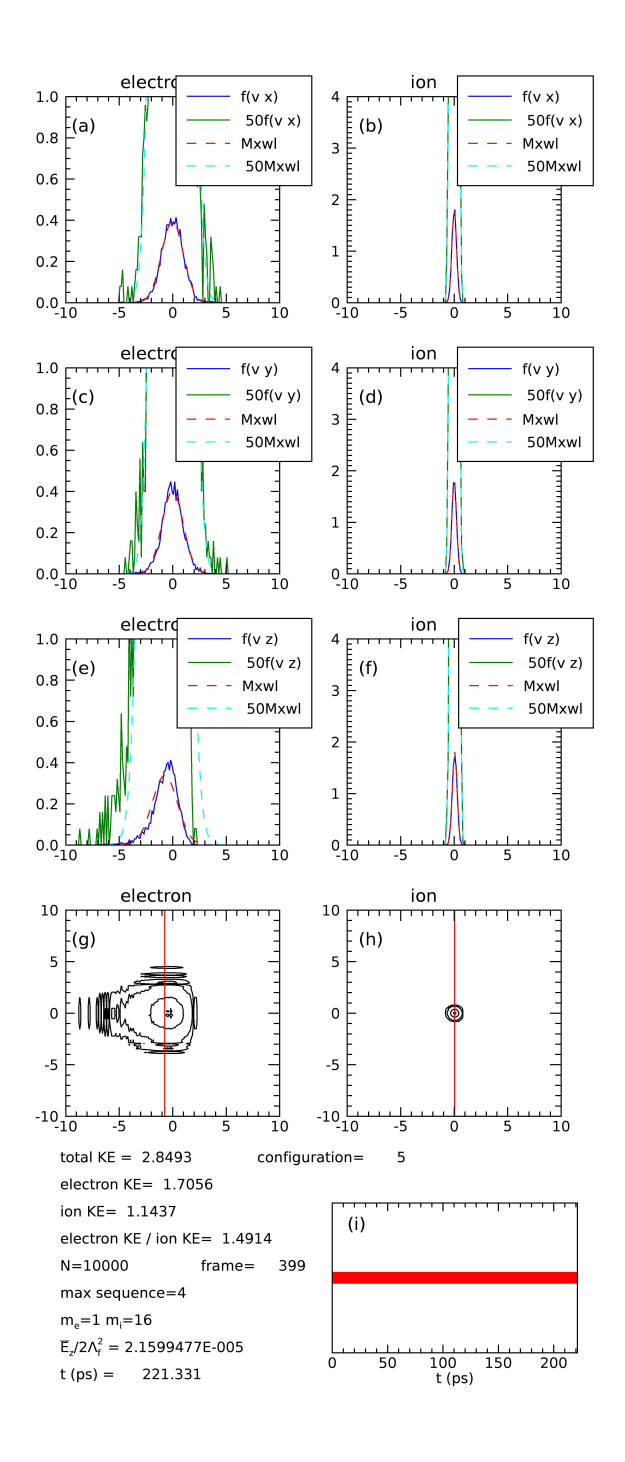


FIG. 9. Configuration #5. Same as Fig. 7 except $\delta_{crit} = 0.2$ (still figure is last figure of animation). (Multimedia view)

numerical iterations are required to capture the effect. The demonstration of the energetic electron tail in Fig. 7(e) and (g) (Multimedia view) and in Fig. 9(e) and (g) (Multimedia view) is the most important result presented in this paper as this tail is qualitatively consistent with experimental observations and not previously predicted.

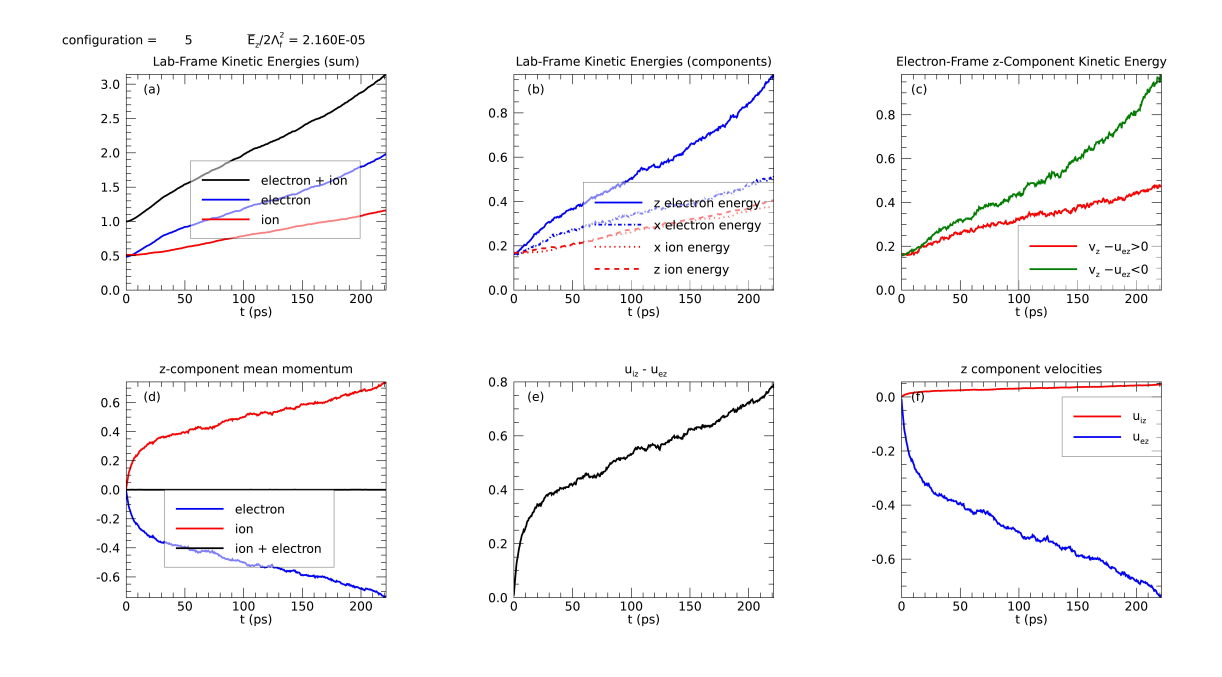


FIG. 10. Configuration #5. Same as Fig.8 except $\delta_{crit} = 0.2$

It is reasonable to conclude that the main energy loss channel is line radiation for the following reasons. At 2 eV, the Ohmic heating power is $E^2/\eta \approx 2 \times 10^{13}$ W m⁻³ while the radiated power in an Argon plasma³² is $P/(n_e n_{Ar}) \approx 5 \times 10^{-31}$ W m³ so for $n_e = n_{Ar} = 10^{22}$ m ⁻³ the radiated power is of order 10^{13} watts. Thus, the radiated power is the same order of magnitude as the Ohmic power. In contrast, using Eq. 15.10 in Miyamoto³³ it is seen that the bremsstrahlung power is 2×10^6 W m⁻³, i.e., seven orders of magnitude smaller than the Ohmic heating power. Furthermore, bremsstrahlung does not have the quantized nature of line radiation and so cannot result in a distinction between particles that collide inelastically and those that do not.

The red lines in Figs. 8(c) and 10 (c) show electron z direction kinetic energy as measured in the electron center of mass frame for $v_z - u_{ez} > 0$ while the green lines show this electron frame kinetic energy for $v_z - u_{ez} < 0$. If the electron distribution were to be a shifted Maxwellian, the green and red lines would be identical so any deviation between the red and green lines indicates deviation from being a shifted Maxwellian. The green to red line ratio gives an indication of the strength of the energetic electron tail as measured in the center of mass frame (lab frame). The increase of the green line relative to the red line shows that the energy of the electron tail is rapidly increasing. Electrons with $\bar{v} > \bar{v}_{crit}$ but having $\delta < \delta_{crit}$ do not have inelastic binary encounters and will be accelerated into even higher energy by the electric field. Unlike Rutherford scattering, the inelastic collision cross-section for ion excitation is a true hit-or-miss cross-section and so plays

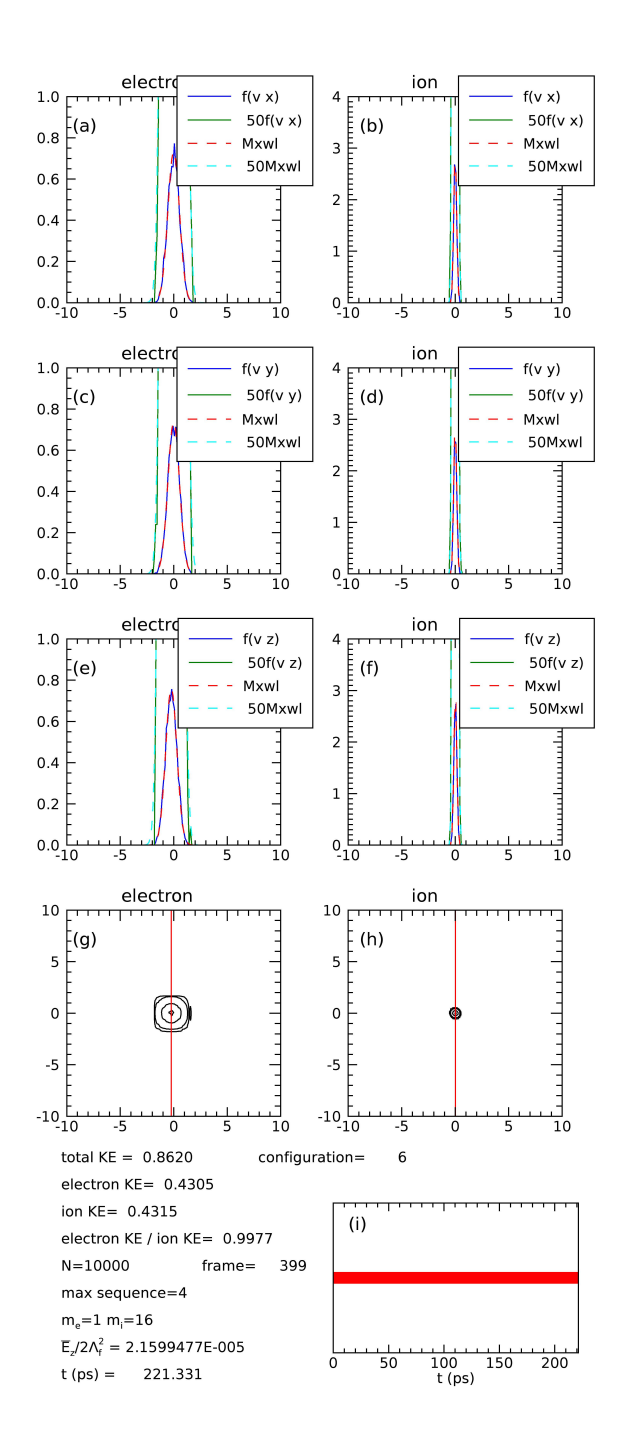


FIG. 11. Configuration #6. Same as Fig. 7 except $\delta_{crit} = 0.03$ (still figure is last figure of animation). (Multimedia view)

the role of the collision cross-section proposed in Sec.II B. Thus, similar to what was proposed by Marshall and Bellan² there will be a small, decreasing in number, subset of 'survivor' electrons that never lose energy because these 'lucky' subset electrons always have $\delta < \delta_{crit}$. This subset of 'survivor' electrons will be accelerated to very high energy and would explain the hard x-rays

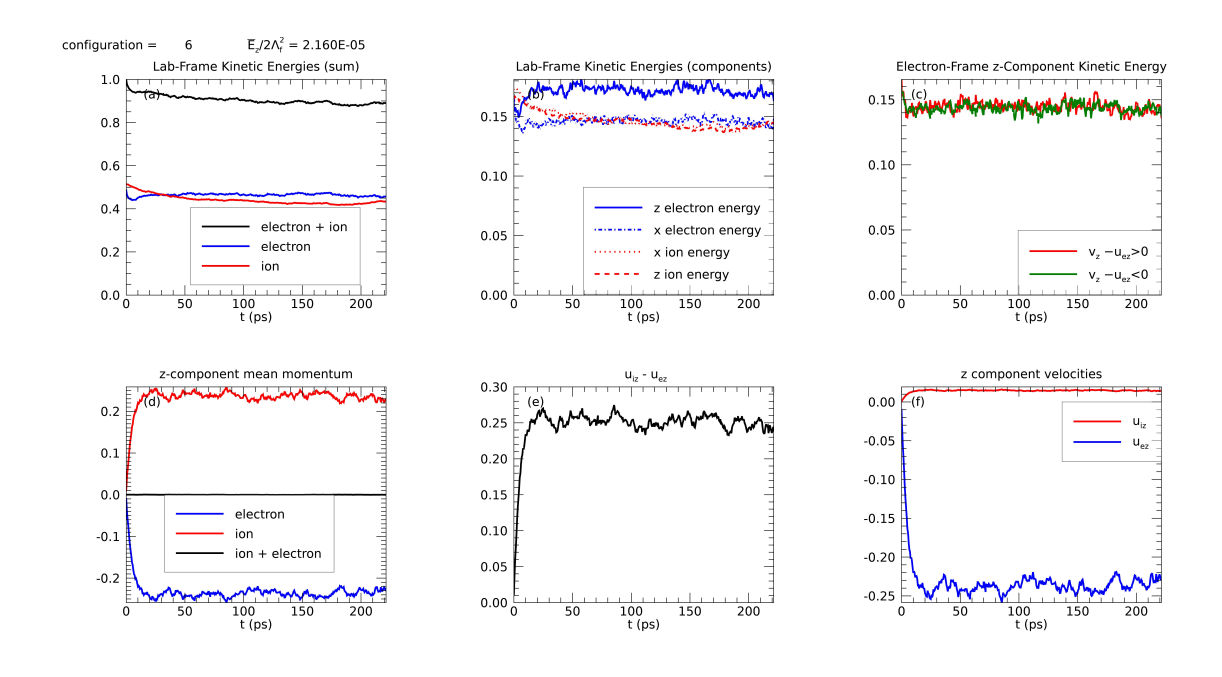


FIG. 12. Configuration #6. Same as Fig.8 except $\delta_{crit} = 0.03$

seen in the Caltech experiment. Configuration #5, shown in Figs. 9 (Multimedia view) and 10, has an approximately 2× larger cross-section for inelastic collisions than configuration #4 so now there are fewer 'survivor' electrons; the energetic electron tail is very clear in Fig.9 (e) and (g) (Multimedia view). Configuration #6, shown in Figs. 11 (Multimedia view) and 12 has a 100× larger cross-section than configuration #4 and so no 'survivor' electrons are evident and the rate at which energy is lost by photon emission balances the rate at which energy is injected by the electric field so what appears to be a steady-state develops; if a much larger number of particles N had been used (e.g., $N = 10^7$), it is presumed that a very small number of 'survivor' electrons would then exist and a tiny deviation from steady-state would be evident. The complete overlap of the dashed red and solid blue lines in Figure 11 (e) (Multimedia view) indicates that the electron velocity distribution is a shifted Maxwellian as prescribed by Eq.A.6 and not a Maxwellian plus perturbation as prescribed by Eq.A.4; this conclusion is supported by Fig.12 (c) which shows that the energies of the forward and reverse z-directed electrons relative to the electron center of mass velocity are equal. A steady-state could develop for configuration #4 if an additional loss mechanism were added that would remove very fast 'survivor' electrons and replace these fast electrons with low-energy electrons. A possible scenario would be that the very fast 'survivor' electrons escape from the volume under consideration faster than the slow bulk electrons and are replaced by a source of low-energy electrons.

A. Time interpretation of numerical results

The un-normalized duration of a binary encounter of an electron moving at the reference velocity is $n^{-1/3}/v_0 = 5.53 \times 10^{-14}$ s for the Caltech experiment. The time step for the numerical integration is $\Delta t = n^{1/3}/(\beta v_0)$ where $\beta = 10$ has been used so as to enable calculation of the probability that a binary encounter occurs in the time Δt ; this value of β has been chosen so that it encompasses the maximum electron velocities in the plots of velocity distribution functions. Thus, $\Delta t = 5.53 \times 10^{-15}$ s so a sequence of Eq.70 with $N = 10^4$ corresponds to each particle (electron or ion) making N - 1 time steps. For example, this would be electron e0 running down the left-most column of the matrix in Eq.68 and so having encounters with each of the N - 1 other particles Thus, the elapsed time for each sequence is $t_{seq} = Nn^{1/3}/(\beta v_0) = 55$ ps so four sequences is 220 ps. The distance a reference electron travels in one sequence would be $v_0 t_{seq} = 44 \mu m$.

B. Energy ratios

If there is no power loss mechanism, the total kinetic energy continuously increases and eventually the rate of electron kinetic energy is m_i/m_e times that of ion kinetic energy. This is consistent with the power inputs into electron and ion kinetic energies being

$$\frac{d}{dt} \left(\frac{1}{2} m_i v_i^2 \right) = q_i \mathbf{E} \cdot \mathbf{u}_i \tag{79}$$

$$\frac{d}{dt}\left(\frac{1}{2}m_e v_e^2\right) = q_e \mathbf{E} \cdot \mathbf{u}_e. \tag{80}$$

The electric field does not change the total plasma momentum which was initially zero so $m_i \mathbf{u}_i + m_e \mathbf{u}_e = 0$. Thus, using $\mathbf{u}_e = -m_i \mathbf{u}_i / m_e$ and $q_i = -q_e$ it is seen that

$$\frac{d}{dt}\left(\frac{1}{2}m_e v_e^2\right) = -\frac{m_i}{m_e} q_e \mathbf{E} \cdot \mathbf{u}_i = \frac{m_i}{m_e} \frac{d}{dt} \left(\frac{1}{2}m_i v_i^2\right)$$
(81)

showing that the electron kinetic energy increases faster than the ion kinetic energy by m_i/m_e as observed in the numerical calculations when there is no radiation. This m_i/m_e ratio of electron to ion energy is observed when the calculation is run for very long times with no radiation. As seen from configuration #3, at very long times most of the kinetic energy is in electron center of mass motion in the z direction rather than in thermal motion so $u_{ez} \rightarrow q_e E_z t/m_e$ and the kinetic energy at long times will be $m_e v_e^2/2 \rightarrow q_e^2 E_z^2 t^2/2m_e$. This t^2 scaling of the z component kinetic energy and the corresponding t scaling of u_{ez} are seen in Figs.20(b) and (f) in Appendix C. This $m_e u_{ez}^2/2$

kinetic energy is not accounted for in Eq.16 and this omission is presumably why the increase in total kinetic energy with no power loss mechanism is faster than predicted by Eq.16.

IX. RELATION TO TOKAMAK RUNAWAY MODELS

Because runaway generation is an important concern for tokamaks, there is an extensive tokamak literature on this topic (e.g., review articles by Knoepfel and Spong³⁴ and by Breizman et al. 35). However, the tokamak situation differs from the Caltech jet experiment in several important ways: (i) because of the excellent confinement in tokamaks, tokamak electrons are accelerated over a distance orders of magnitude longer than the characteristic device size whereas in the Caltech jet experiment the electron acceleration is a single pass through the length of a portion of the plasma; (ii) tokamak runaway electrons are relativistic, are a significant fraction of all the electrons, and carry a significant fraction of the electric current whereas in the Caltech jet experiment the energetic tail electrons are non-relativistic, are a tiny fraction of all the electrons, and carry a negligible fraction of the current; (iii) a tokamak has a relatively constant or slowly changing electric field whereas in the Caltech jet experiment the electric field abruptly turns on because of a sequence of MHD instabilities. The model presented here describes the consequences of an abruptly-created, very large electric field in a device with modest confinement and so differs from the tokamak situation of a long-lasting small electric field in a device having near-perfect confinement. The Caltech jet experiment may however have a relationship to the rapid generation of energetic particles during tokamak reconnection instabilities such as a sawtooth crash since a strong transient electric field is typically produced in these instabilities. The Caltech jet experiment is also likely related to generation of energetic particles in a solar reconnection event as discussed in Zhang et al. ²⁶, Marshall et al. ¹, and Marshall and Bellan ².

X. SUMMARY

This paper is motivated by experimental observations of 6 keV X-rays in a plasma that is so cold (2 eV) and collisional that one would not expect any electron to be accelerated to 6 keV and so produce an X-ray. These X-rays were short bursts at the end of a cascading sequence of qualitatively different types of instabilities (kink, Rayleigh-Taylor, and presumed collisional Buneman). A previous model attempted to explain the production of 6 keV electrons by proposing

that, in analogy to a lucky soldier who goes through many battles without being wounded, there is a tiny sub-group of "lucky" electrons that never collide and so attain a large directed kinetic energy in the presence of an electric field. However, this previous model was discredited on the grounds that all electrons are the same (no lucky subgroups) because electron collisions in a plasma involve the cumulative effect of a large number of grazing collisions, rather than a hit or miss process. The electric field was inferred to be smaller than the Dreicer field, which is the field for all electrons to run away and attain high energy, so the experimentally observed process is not consistent with a classic run-way situation as only a tiny number of electrons have high energy.

The paper presents a numerical model that differs from prior work because, unlike prior work, there is no explicit analytic averaging over impact parameters, that is, there is no explicit invocation of a Coulomb logarithm. Instead, a large number of encounters between particles is evaluated with varied impact parameters, interspersion of e-e, e-i, and i-i encounters, and use of the continuously changing direction of the trajectory of particles rather than the traditional assumption that a particle has an unchanged direction while summing up the consequences of a large number of encounters. The analysis takes into account that superthermal particles are not Debye shielded because they move too fast for Debye shielding to be established. Instead it is shown (with detailed argument in Appendix B) that for superthermal particles the effective cutoff for an averaging over impact parameters is the interparticle distance rather than the Debye length. It is further shown that this leads to a Coulomb logarithm scaling as $\ln\left(4\pi\left(n\lambda_D^3\right)^{2/3}\right)$ instead of $\ln\left(4\pi\left(n\lambda_D^3\right)\right)$ which makes little difference since the ratio of these quantities is 2/3 when $n\lambda_D^3$ is very large. The numerical code divides space into scattering cubes having side dimensions equal to $n^{-1/3}$, the interparticle spacing. A field particle is assumed to be at a random location in each scattering cube so the density of field particles is n. The scattering calculation is done for a small time interval Δt defined by the time it takes for a particle having ten times thermal velocity to traverse a scattering cube. This means that a particle with velocity $10 v_T$ will traverse the scattering cube in the time interval Δt and so always encounters a field particle, but a particle with velocity v_T , will only traverse one tenth the length of the scattering cube and so only has a 10% chance of encountering a field particle. This procedure is analogous to the classic differential cross-section argument where the number of encounters in a time Δt is presumed to be proportional to a distance $v\Delta t$ multiplied by a cross section $d\sigma$ multiplied by a density of field particles. However, this procedure is more accurate because it takes into account the changing of the direction of the test particle after each encounter and the interspersion of different types (e-e, e-i, etc.) of encounters. The numerical results show

that when there is no electric field, a classic 3D Maxwellian thermalized velocity distribution is established on an expected time scale such that electrons thermalize first, then ions, and then electrons and ions come to the same temperature. A simple analytic argument shows that if there is no power loss mechanism, then when an electric field is applied to a plasma, no equilibrium can result and instead the plasma rapidly heats up to very high temperature and runs away as the condition for runaway goes inversely with temperature. It is then shown that equilibria can occur if there is a heat loss mechanism but the equilibrium will depend on the type of loss mechanism and so will not be unique. A specific type of loss mechanism is considered, namely optical radiation, as would occur when an energetic electron comes very close to an ion and so excites a bound electron attached to the ion to a sufficiently high energy state for a photon to be radiated. It is shown that this mechanism corresponds to a well-defined cross-section so it is now possible for there to be a subset of lucky electrons that never come close enough to an ion with sufficient energy to cause photon emission. These lucky electrons will be continuously accelerated in the presence of an electric field and will attain sufficient energy to generate x-rays when they finally make an exceedingly rare large angle collision. The numerical calculation also shows that when radiation is allowed but the electric field is weak, then a near-equilibrium can be established and that this equilibrium is such that the electron distribution function is a shifted Maxwellian. This is an important point because typical analytic models of collisions are based on the postulate that the electron distribution function is not a shifted Maxwellian but instead is an unshifted Maxwellian plus a small perturbation.

XI. CONCLUSION

There is a logical inconsistency in assuming that an isolated plasma can be in a steady-state when there are collisions and a finite electric field because the plasma will continuously heat up as there is no place for the injected energy to go. To have a steady state there must be a mechanism for removing energy at the rate it is being injected. Several different types of loss mechanism are possible but the likely loss mechanism for the Caltech jet experiment and probably many other situations is atomic line radiation. This is consistent with the experimental observation by Chai et al³⁶ of ion excitation and higher ionization states during the same kink-driven Rayleigh-Taylor instability that exhibited x-ray emission. For low-strength electric fields competing with this radiative loss mechanism, an equilibrium can develop and this equilibrium has the form of a shifted

Maxwellian. However, higher strength electric fields that are still sub-Dreicer will produce energetic electron tails and distribution functions very different from a shifted Maxwellian. These energetic tails are more consistent with experimental observations than the predictions of a shifted Maxwellian and cannot be modeled by a Maxwellian plus perturbation because the assumption that the perturbation is small compared to an unshifted Maxwellian is invalid for a high-energy non-Maxwellian tail. It is the quantum hit-or-miss nature of the electron excitation of ions that produces a true cross-section so that it is possible to have an electron that continuously fails to excite ions while simultaneously gaining more and more energy from the electric field. Such "survivor" electrons will be few in number, but they will exist and so will constitute a highly energetic tail that could produce x-rays. This model suggests that if there is no heat conduction or particle loss (two other possible ways to balance the power input from the electric field) then radiation provides the temperature limit so if there is very little radiation, then a very high temperature results. This is of course well known for tokamaks where the emphasis on vacuum cleanliness is to reduce radiative loss that would limit the temperature. The radiation model presented here is a toy model that demonstrates the essential dynamics in a semi-quantitative manner; i.e., it captures the order of magnitude of what is going on and reveals the competition between major effects but it is not precise. In order to attain a precise quantitative description, account would have to be taken of multiple levels of excitation, ionization, recombination, and the specific, detailed energy dependence of excitation and ionization cross-sections.

AUTHOR DECLARATIONS

Conflict of Interest

The author has no conflicts to disclose.

Author Contributions

Paul M. Bellan: Conceptualization (lead); Funding acquisition (lead); Formal analysis (lead); Investigation (lead); Methodology (lead); Project administration (lead); Supervision (lead); Validation (lead); Original draft preparation (lead); Review and editing (lead).

ACKNOWLEDGMENTS
Supported by NSF Award Number 2105492 and AFOSR Award Number FA9550-21-1-0379.
DATA AVAH ADH ITV CTATEMENIT
DATA AVAILABILITY STATEMENT
Raw calculated velocity distributions will be posted on the Caltech archival server https://data.caltech.edu

APPENDIX A. DIFFICULTIES WITH PREVIOUSLY USED MODELS OF RESISTIVITY AND COLLISIONS

The concepts and assumptions underlying previously used models of plasma resistivity and collisions satisfactorily describe many situations. However, there are difficulties with these traditional models which will be scrutinized in this appendix.

The theory of plasma resistivity necessarily involves a competition between acceleration produced by an electric field and drag produced by collisions. As stated in the main text of this paper, e-e collisions tend to make the electrons Maxwellian in the center of mass frame of the electrons whereas e-i collisions tend to make the electrons isotropic in the ion frame. These tendencies are in situations where there is no electric field. It is instructive to examine the complementary situation, namely what happens when there is an electric field, but no collisions. To do this, consider the situation of a plasma that initially has no electric field and then an electric field is suddenly applied and where the electric field is the only effect. The Vlasov equation is now collisionless and time-dependent with the form

$$\frac{\partial f_{\sigma}}{\partial t} + \frac{q_{\sigma}}{m_{\sigma}} \mathbf{E} \cdot \frac{\partial f_{\sigma}}{\partial \mathbf{v}} = 0. \tag{A.1}$$

This has the solution

$$f_{\sigma}(\mathbf{v},t) = f_{\sigma} \left(\mathbf{v} - \frac{q_{\sigma}}{m_{\sigma}} \mathbf{E}t \right)$$
 (A.2)

since $\mathbf{v} - \frac{q_{\sigma}}{m_{\sigma}} \mathbf{E}t$ is the velocity at t = 0, a constant of the motion, and solutions of the Vlasov equation are functions of the constants of the motion.

If the velocity distribution is Maxwellian at t = 0 then

$$f_{\sigma}(\mathbf{v},t) = \frac{n}{\pi^{3/2} v_{T\sigma}^{3}} \exp\left(-\frac{\left(\mathbf{v} - \frac{q_{\sigma}}{m_{\sigma}} \mathbf{E}t\right)^{2}}{v_{T}^{2}}\right)$$
(A.3)

which shows that to the extent that collisions are not important, the electric field produces a shifted Maxwellian where the shift increases linearly with time.

However, classical models of resistivity assume the solution is time-independent and so, instead of balancing the electric field with the time-dependent term in the Vlasov equation, the electric field force is assumed to balance frictional drag. Two traditional models of plasma resistivity exist and differ by their initial assumptions and by the level of detail at which averaging is done. Both types of models calculate resistivity η via a steady-state Fokker-Planck¹⁷ model that averages the

consequence of a large number of transient Rutherford scattering events. These events, called binary encounters, occur when two charged particles are in close proximity.

The first and more widely used type of model is based on the Chapman-Enskog method and assumes that an electric field **E** causes an electron velocity distribution to become the sum of a Maxwellian $f_{e,0}(v)$ and a perturbation $f_{e,1}(v)$, i.e.,

$$f_e(v) = f_{e,0}(v) + f_{e,1}(v)$$
 (A.4)

where

$$f_{e,1}(v) \ll f_{e,0}(v)$$
 (A.5)

and $f_{e,1}(v)$ is proportional to the electric field. Here the Maxwellian is centered about the plasma center of mass velocity which is essentially the ion center of mass velocity. This model has been used by Cohen *et al.* ¹⁸, by Spitzer and Härm ¹⁹, by Landreman and Ernst ²⁵, and in Sec.13.4 of the text by Goldston and Rutherford ²⁹.

The second type of model starts by presuming that when there is an electric field, the electron and ion velocity distributions are shifted Maxwellians, i.e.,

$$f_{\sigma}(\mathbf{v}) = n \left(\frac{m}{2\pi \kappa T_{\sigma}} \right)^{3/2} \exp \left(-\frac{m_{\sigma} (\mathbf{v} - \mathbf{u}_{\sigma})^{2}}{2\kappa T_{\sigma}} \right). \tag{A.6}$$

This model has been used by Trubnikov²⁰, by Krall and Trivelpiece²¹, and by Bellan²².

While these two types of models differ in important ways, they share the shortcoming that both prescribe a specific mathematical structure for the electron velocity distribution rather than leave this structure undetermined and to be solved for. The Maxwellian plus perturbation model solves the collisional Vlasov equation for each velocity \mathbf{v} whereas the shifted Maxwellian does not do so and instead balances the acceleration produced by the electric field against a frictional drag calculated by averaging over all electron velocities. While the Maxwellian plus perturbation method appears to provide a velocity-by-velocity detailed balance between acceleration and drag, this method suffers from its violating at large electron velocities the assumption given in Eq.A.5. This violation is because the obtained solution predicts that $f_{e,1}(v)/f_{e,0}(v)$ scales as v^4 and so diverges at large velocities (see Eq.13.21 of Goldston and Rutherford ²⁹ and Eq.(47) of Cohen *et al.* ¹⁸). A further issue is that the Maxwellian plus perturbation method refers to an ambiguously-defined electron temperature. Electron temperature is proportional to a mean-square random electron velocity where random velocity is defined as the velocity relative to a center of

mass velocity. The ambiguity is in what is assumed for the center of mass velocity as two possible choices exist, namely the plasma center of mass velocity and the electron center of mass velocity. This discrepancy is important because electron-electron collisions tend to make the electron distribution function become a Maxwellian centered about the electron center of mass whereas electron-ion collisions make the electron distribution function isotropic (but not Maxwellian) with respect to the plasma center of mass velocity, essentially the ion center of mass velocity.

The shifted Maxwellian method presumes that electron-electron collisions make the distribution function Maxwellian in the electron center of mass frame but does not solve the collisional Vlasov equation velocity by velocity. The shifted Maxwellian method is provided in Section 16 of Trubnikov²⁰ where it is used to construct a three-term equation (Eq.16.7 in Trubnikov²⁰) where the respective terms are the bulk electron acceleration, the electric field force, and the drag force. Because the drag force has a velocity-dependent maximum, Trubnikov shows that if the electric field force exceeds this maximum, the time derivative of mean electron velocity cannot be zero. This gives a condition for runaway. Krall and Trivelpiece²¹ and Bellan²² show that if the electric field is much less than this maximum, then the electric field force and drag can balance to provide a steady-state (no bulk electron acceleration). The ratio of electric force to mean relative velocity gives the resistivity in Eq.14. The η calculation is conveniently done in a frame moving with the electron mean velocity \mathbf{u}_e because in this frame, the ions can be considered to be a nearly monoenergetic beam traversing a swarm of thermal electrons having zero mean velocity. This method captures the fact that electrons with different velocities have different drag on ions without violating an assumption that a perturbation in the shape of the electron velocity distribution is small, i.e., without asserting Eq.A.5. The mono-energetic ion assumption is a good assumption because, being heavy, ions have a much smaller thermal velocity spread than electrons. The drag on the ion beam resulting from its interaction with the swarm of thermal electrons takes into account all possible binary ion-electron collisions weighted according to their probability.

Because the shifted Maxwellian method does not allow for alteration of the shape of the electron velocity distribution other than a shift, it cannot predict a tail because the method effectively starts by prescribing that no tail exists. By comparison, the Maxwellian plus perturbation method allows a tail but at large velocities the calculated tail violates the assumption given by Eq.A.5. To see this, consider Eq.(47) in Cohen *et al.* ¹⁸ which is $D = Ax^4$ where x is the normalized velocity, D is the perturbation normalized to a Maxwellian and $A = E/E_D$. Section II gives x = 50 and A = 0.2 so $D = 1.25 \times 10^6$ which violates Eq.A.5 by six orders of magnitude. Spitzer and Härm ¹⁹

extend Cohen *et al.* ¹⁸ to take into account electron-electron collisions and arrive at a result that is slightly different but similarly diverges at large velocities.

Question marks have been placed in Table I for Braginskii ¹⁶ because Braginskii appears to assume shifted Maxwellians for the electrons and ions so the shift in mean velocities would correspond to an electric current. There is no discussion in Braginskii ¹⁶ of an electric field driving this shift (see second sentence after Braginskii's Eq.2.1 and definitions in Braginskii's Eq.1.3). Braginskii ¹⁶ then goes on to assume that a solution to the collision problem is of the form of a shifted Maxwellian with a perturbation to this shifted Maxwellian; this perturbation to the shifted Maxwellian is calculated using the Chapman-Enskog method. Braginskii ¹⁶ does not calculate resistivity but rather is concerned with viscosity and heat transport.

According to Arber *et al.* ¹⁵, a method proposed by Takizuka and Abe ¹⁴ is commonly used in Particle-in-Cell (PIC) codes to describe collisions and, at first sight, the Takizuka and Abe method appears similar to that presented in this paper. However, the method prescribed by Eq.67 in this paper for choosing impact parameter b which then determines δ is advocated as being physically more realistic than the Takizuka and Abe method. This is because Takizuka and Abe do not calculate individual binary encounters with a specified b but, instead, for each binary encounter δ^2 is chosen arbitrarily with a Gaussian distribution that depends in a rather circular fashion on analytic estimates of collision properties involving quantities such as $\ln \Delta$. The quantity δ is a parameter characterizing a single binary encounter and so cannot depend, as was assumed by Takizuka and Abe, on averaging over a large number of binary encounters. The quantity $\ln \Delta$ is calculated by averaging over a large number of impact parameters and so cannot be used to describe what happens in single binary encounter where there is a single, specific, fixed impact parameter.

APPENDIX B. DETAILED JUSTIFICATION FOR WHY INTERPARTICLE DISTANCE IS USED AS CUTOFF FOR SUPERTHERMAL PARTICLES

The traditional derivation of particle collisions in a plasma involves Debye shielding, a phenomenon the derivation of which depends on assuming thermal equilibrium (e.g., see third sentence of Sec.1.7 in Goldston and Rutherford 29). However, thermal equilibrium requires collisions so the argument is circular as collisions are required to establish the conditions for collisions. This circularity constitutes a logical weakness in the argument as circular arguments can be false. The derivation of Debye shielding combines Poisson's equation and Boltzmann solutions (the latter a consequence of thermal equilibrium) to show that a particle "A" with charge q_A located at the origin has a Yukawa-type potential

$$\phi_{Yuk}(\mathbf{r}) = \frac{q_A e^{-r/\lambda_D}}{4\pi\varepsilon_0 r}.$$
 (B.1)

The assumptions of thermal equilibrium, slowness, and derivation of the Yukawa potential are given in Sec.1.2 of Nicholson ²⁸.

The Rutherford scattering angle θ , given by Eq.8, is based on a computation involving a potential having the form $\phi = q_A/4\pi\epsilon_0 r$ and not that given by Eq.B.1. The analysis of collisions does not use Eq.B.1 but, in the process of evaluating the range of impact parameters to use in the Rutherford scattering computation, instead makes the "ad hoc" approximation that

$$\phi(\mathbf{r}) = \begin{cases} \frac{q_A}{4\pi\varepsilon_0 r} & \text{for } r \leq \lambda_D \\ 0 & \text{for } r > \lambda_D; \end{cases}$$
(B.2)

the potential is said to be "cut off" at $r = \lambda_D$. This potential is sketched in Fig.13. It is stated that the vacuum potential (top line of Eq.B.2) is "cut off" at $r = \lambda_D$ so that Rutherford scattering at impact parameters larger than λ_D is discarded. The corresponding electric field is

$$\mathbf{E}(\mathbf{r}) = \begin{cases} \frac{q_A}{4\pi\varepsilon_0 r^2} \hat{r} \text{ for } r \leq \lambda_D \\ 0 \text{ for } r > \lambda_D. \end{cases}$$
(B.3)

According to electrostatic theory, Eq.B.2 corresponds to assuming that for $r \leq \lambda_D$ there are *no* particles other than particle "A", i.e., it is assumed that there is perfect vacuum between particle "A" at r=0 and a shell of charge at $r=\lambda_D$; this is shown in Fig.14. The shielding cloud is, as sketched in Fig.14, a shell at $r=\lambda_D$ with a surface charge density $\sigma_{sc}=-q_A/4\pi\lambda_D^2$. This shell

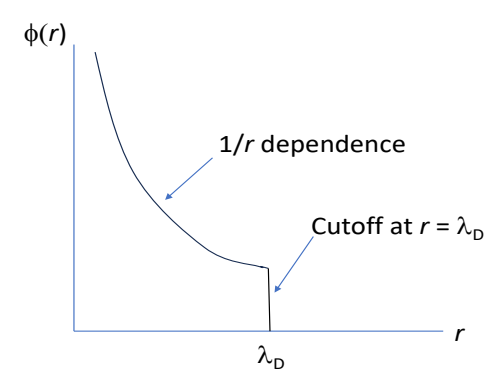


FIG. 13. Electrostatic potential with cutoff at Debye length plotted as function of radius.

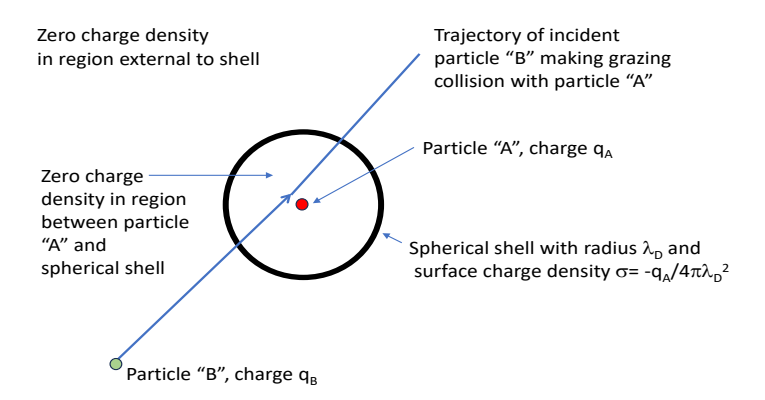


FIG. 14. Charge distribution corresponding to particle "A" electrostatic potential with cutoff and trajectory of particle "B" making a grazing collision with particle "A".

surface charge is presumed to correspond to the time-average of motions of non-"A" particles in the vicinity of particle "A". Since the total charge on this surface is equal and opposite to that of particle "A", each small segment of the surface is thus assumed to have a small fraction of a charge, an assumption which is non-physical if time averaging is not invoked, since fractional charges do not exist.

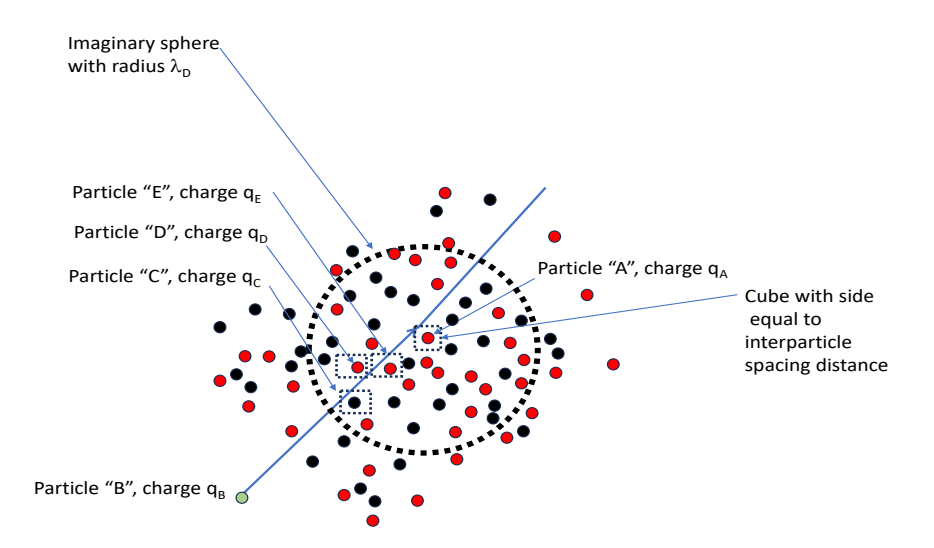


FIG. 15. Randomly located particles with Debye length shown as dotted circle. Fast particle "B" makes close encounters with discrete particles "C", "D" and "E" as well as with particle "A".

Consider now a binary encounter between some other particle, labeled "B", and particle "A" where the Debye shielding of particle "A" is approximated by Eq.B.2. For simplicity, we assume that particle "A" is much heavier than particle "B" so it is not necessary to transform to center of mass coordinates. The trajectory of particle "B" is shown by the blue slanted line in Fig.14; the slant angle changes slightly as the result of the encounter and this change is a grazing or smallangle encounter. When particle "B" is at a radius $r > \lambda_D$, the electric field it experiences is zero and so it experiences no force. When particle "B" is at $r < \lambda_D$ it experiences only the vacuum electric field from particle "A", i.e., the situation is modeled as if particle "A" is surrounded by vacuum up to $r = \lambda_D$. In neither the case $r < \lambda_D$ nor the case $r > \lambda_D$ can it be said that particle "B" simultaneously interacts with all of the millions of particles that on time-averaging form the shielding cloud. The effect of the shielding particles is simply to cut off the potential of particle "A". One might argue that particle "B" is interacting with both particle "A" and the shielding cloud in such a way that the net interaction is zero. However, this would be contrary to the usual meaning of the word 'interact', because one does not usually use this word to describe an electron passing a neutral particle; that is, one does not state that the electron feels both a force from the nucleus of the neutral particle and a force from the electrons surrounding this nucleus and that these forces happen to cancel each other.

It takes a time ω_{pe}^{-1} to establish a Debye shielding cloud so as discussed in Sec.II C, if particle

"B" is superthermal there is insufficient time for a Debye shielding cloud to be established. In this case, particles other than particle "A" will be randomly located. This randomness means that the other particles do not form a thin uniformly charged shell as sketched in Fig. 14. This real situation is instead as sketched in Fig.15 where it is seen that fast particle "B" comes within an interparticle spacing (denoted by small box) of particles "C", "D" and "E" as well as coming close to particle "A". When particle "B" is much less than the interparticle separation distance from particles "C", "D" and "E", particle "B" will experience a very strong electric field from each of "C", "D" and "E". Of course, particle "B" will also experience electric fields from all the other particles but these other particles are randomly located in all directions from particle "B" so the force produced by each of these other particles will be in a random direction. When these randomly directed forces are summed, the result will be zero. As an intuitive example, consider a comet being deflected by the sun. The nearest other star is five light years away and assume that this is the typical interstellar distance. Each of the multitude of stars in the universe produces a gravitational force on the comet so the comet experiences the gravitational force of the sun plus the gravitational forces of all other stars in the universe. Gravitational force is an inverse square force like the Coulomb force. The forces from the other stars are weak because the other stars are far way. Each distant star produces a force in a different random direction so that when these distant star forces are summed, the result is negligible compared to the gravitational force of the sun. Thus, the comet only feels the gravitational force of the sun. Whether the comet makes a grazing or a large angle collision depends on how fast the comet is going and its impact parameter. The interaction between the comet and the sun can thus be considered to be a binary interaction as the forces from the other stars have negligible effect.

In a plasma with randomly located particles (process too fast for Debye shielding to be established), a test particle experiences a force from the particle that is less than an interparticle distance away but not from particles at greater distances. This means that Debye shielding with the cutoff approximation specified by Eq.B.2 results in a force field having a *greater extent* than when there is no Debye shielding. The interparticle spacing distance $n^{-1/3}$ is less than the Debye length λ_D since $n\lambda_D^3 \gg 1$ is presumed. Consequently, the conventional Coulomb logarithm derivation with its Debye shielding cutoff argument effectively *extends* the range of the potential of particle "A" compared to when there is no Debye shielding. This is contrary to the commonly held presumption that Debye shielding shortens the range of the potential. Debye shielding shortens the range relative to that of a single particle in vacuum but extends the range compared to the range of the

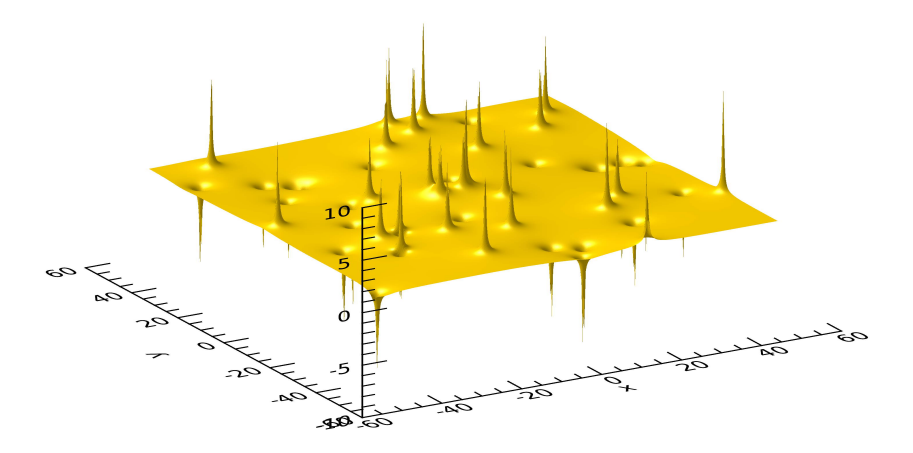


FIG. 16. Plot of potential of 25 randomly located ions and 25 randomly located electrons in a 2D plane. This potential is calculated numerically using Eq.B.4. A fast particle traversing this system would experience the electric field of each spike one at at time when it is in the vicinity of each spike. The potential in the regions between spikes is flat so there is no electric field in the region between the spikes.

potential of a single particle surrounded by a large number of randomly located other particles.

Figure 16 shows the numerically evaluated electrostatic potential of 25 randomly located positive and 25 randomly located negative charges located in an x-y plane at fixed positions $\{x_j, y_j\}$; this potential is given by

$$\phi(x,y) = \sum_{j=1}^{N} \frac{q_j}{\sqrt{(x-x_j)^2 + (y-y_j)^2}}$$
 (B.4)

where $q_j = +1$ for positive particles and $q_j = -1$ for negative particles. This figure shows that the potential is a sharp spike when $\{x,y\}$ is close to $\{x_j,y_j\}$ and is near zero elsewhere because away from a spike, the contributions from the various positive and negative particles nearly cancel (the figure is done in a 2D system so the potential can be plotted in the vertical direction; potentials in a 3D system would be similarly spiky but would not be so easily visualized since a fourth dimension would be needed for plotting). The electric field is the gradient of the potential and so is very large near each spike but is near zero elsewhere. A fast charged particle traveling through this potential system would only experience an electric force when near a spike and so would only be deflected when near a spike. This would be a binary encounter. If $n\lambda_D^3 \gg 1$, then $\lambda_D \gg n^{-1/3}$ so the Debye length is much larger than the interparticle spacing.

The impossibility of Debye shielding of a superthermal particle will now be shown using a reductio ad absurdum argument where it is initially assumed that a superthermal particle "B" passes through a Debye sphere shielding a particle "A". The fast incident particle "B" traveling a Debye length would pass many fixed spikes in Fig.16 and because particle "B" is superthermal, the field particles are in fixed positions during the time particle "B" traverses the Debye sphere. If one spike was selected as being the potential of particle "A", it seen that particle "B" would be deflected by many of the non-"A" spikes before it reached the spike of particle "A". If there were indeed millions of particles within a Debye sphere, then on traversing the Debye sphere, and so traversing a Debye length, particle "B" would come close to some significant number of these millions of particles. To estimate how many particles particle "B" comes close to, consider a cylinder with axis given by the trajectory of particle "B" (slanted blue line in Fig.15) and with radius equal to the interparticle spacing $n^{-1/3}$. Any field particle within this cylinder would be less than an interparticle spacing from the trajectory of particle "B" while particle "B" is in the Debye sphere. The volume of this cylinder is $\lambda_D \pi n^{-2/3}$ so the number of field particles in this cylinder is $\lambda_D \pi n^{1/3} \approx (n \lambda_D^3)^{1/3}$. This means that if there are millions of field particles in a Debye sphere, particle "B" will come within the interparticle distance of the spikes of hundreds of non-"A" particles before encountering the spike of particle "A". Thus, particle "B" encounters the spikes of hundreds of stationary non-"A" particles which contradicts the assumption that particle "B" travels in a straight line without deflection through the Debye shielding cloud except for being deflected by the spike of particle "A". This contradiction indicates that for superthermal particles the cutoff should be at the interparticle spacing rather than at the Debye length. However, Eq. 20, shows that this makes little difference because of the logarithmic dependence.

APPENDIX C. DEPENDENCE ON ELECTRIC FIELD STRENGTH

These additional figures referred to in the main text have different $\bar{E}_z/2\Lambda_f^2$ from related figures in the main text and show the scaling with \bar{E}_z .

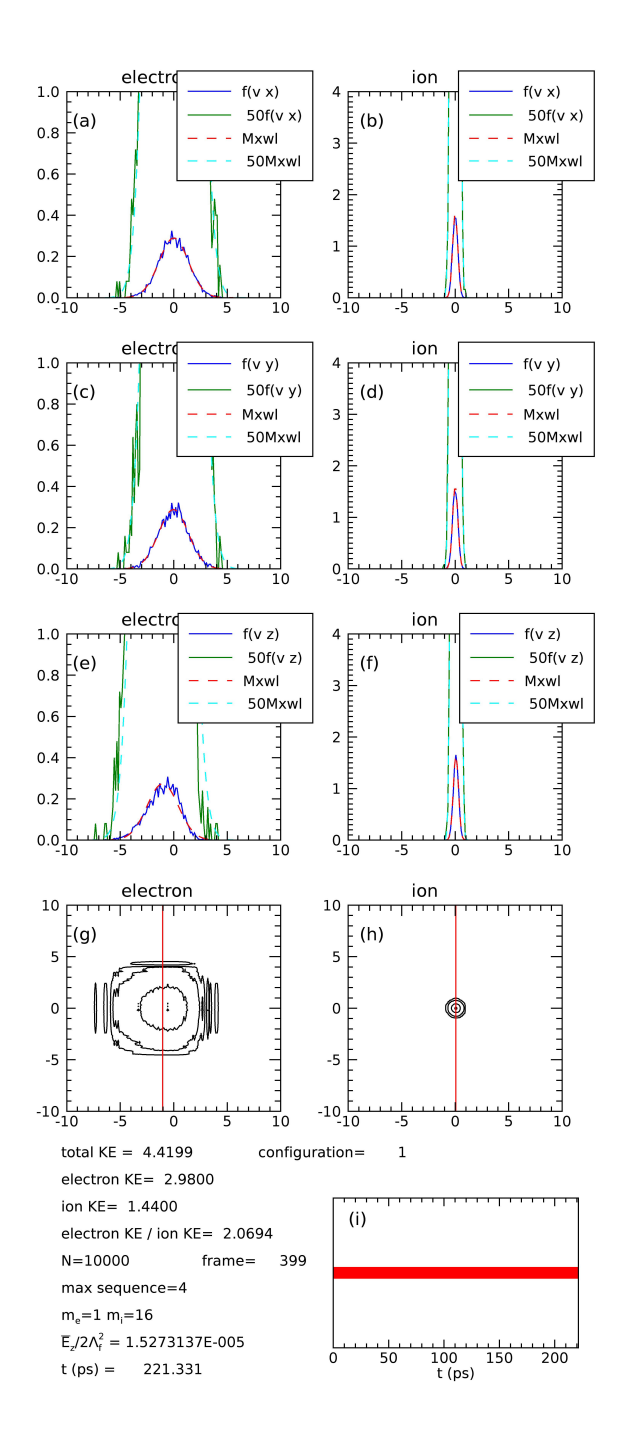


FIG. 17. Configuration #1. Velocity distribution evolutions (still figure is last figure of animation). $\bar{E}_z/2\Lambda_f^2=1.53\times10^{-5}$ and no radiation. (Multimedia view)

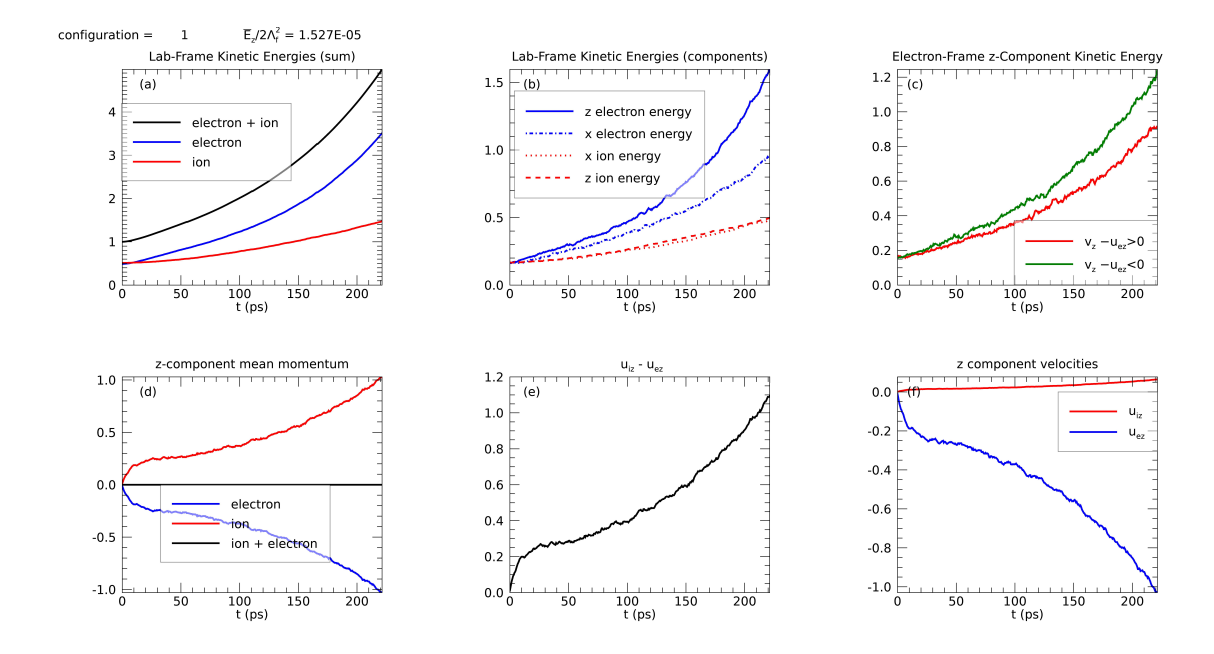


FIG. 18. Configuration #1. (a) Lab-frame kinetic energies for sum of all direction components, (b) lab-frame kinetic energy of z and x components (y same as x), (c) electron-frame kinetic energy z components in positive and negative directions (note that these are not equal contrary to assumption in Eq.A.6 and also no equilibrium is achieved), (d) shows that momentum is conserved, (e) shows that $u_{i,z} - u_{e,z}$ increases without bound (i.e., current density increases without bound), (f) shows that $u_{i,z}$ and $u_{e,z}$ increase without bound.

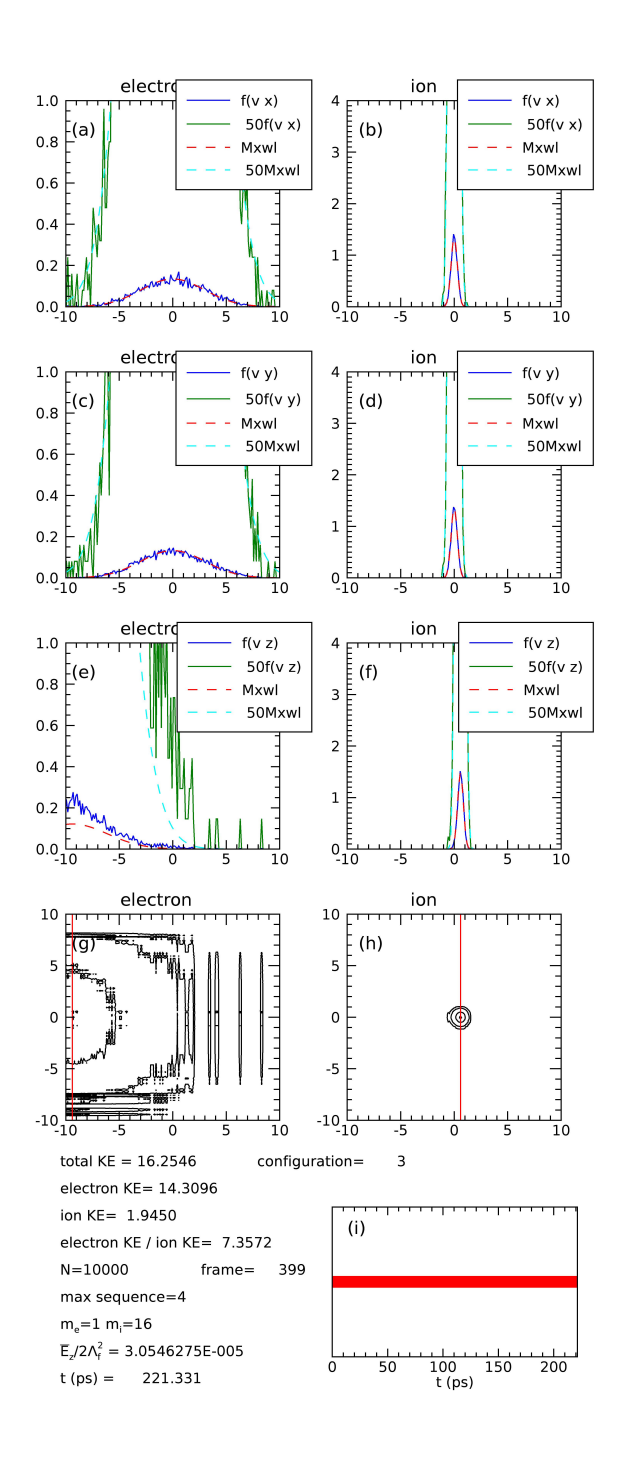


FIG. 19. Configuration #3 evolution of velocity distributions (Multimedia view).

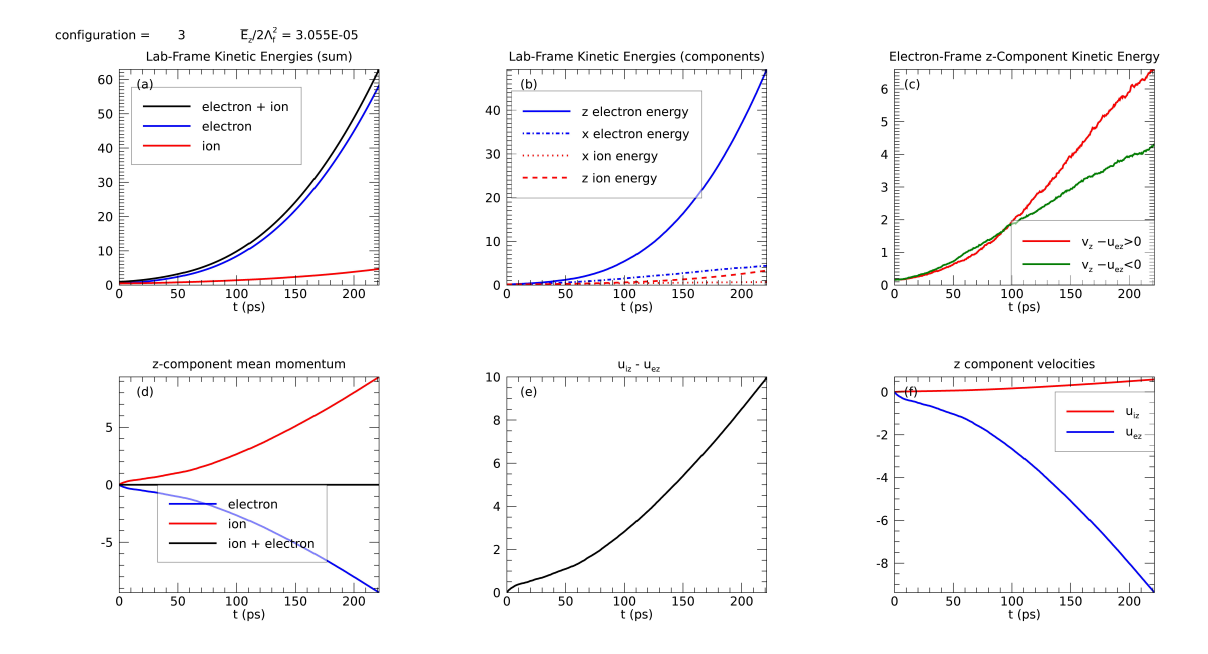


FIG. 20. Configuration #3 energies and momenta. (a) and (b) show that electron energy is mainly in the z direction and increases as t^2 . (f) shows that u_{ez} increases linearly with time.

REFERENCES

- ¹R. S. Marshall, M. J. Flynn, and P. M. Bellan, Physics of Plasmas 25, 112101 (2018).
- ²R. S. Marshall and P. M. Bellan, Physics of Plasmas **26**, 042102 (2019).
- ³M. J. Aschwanden, Space Science Reviews **101**, 1 (2002).
- ⁴W. G. Pilipp, H. Miggenrieder, M. D. Montgomery, K. H. Mühlhäuser, H. Rosenbauer, and R. Schwenn, Journal of Geophysical Research **92**, 1075 (1987).
- ⁵F. Fiuza, G. F. Swadling, A. Grassi, H. G. Rinderknecht, D. P. Higginson, D. D. Ryutov, C. Bruulsema, R. P. Drake, S. Funk, S. Glenzer, G. Gregori, C. K. Li, B. B. Pollock, B. A. Remington, J. S. Ross, W. Rozmus, Y. Sakawa, A. Spitkovsky, S. Wilks, and H.-S. Park, Nature Physics **16**, 916 (2020).
- ⁶D. F. d. Cruz, A. G. Peeters, A. J. H. Donne, N. J. L. Cardozo, and E. Westerhof, Plasma Physics and Controlled Fusion **35**, 693 (1993).
- ⁷Y. Zhou and P. M. Bellan, Physics of Plasmas **30**, 052101 (2023).
- ⁸S. You, G. S. Yun, and P. M. Bellan, Physical Review Letters **95**, 045002 (2005).
- ⁹P. M. Bellan, Physics of Plasmas, 055601 (2018).
- ¹⁰A. L. Moser and P. M. Bellan, Nature **482**, 379 (2012).
- ¹¹O. Buneman, Physical Review Letters **1**, 8 (1958).
- ¹²H. Dreicer, Physical Review **117**, 329 (1960).
- ¹³R. M. Kulsrud, Y.-C. Sun, N. K. Winsor, and H. A. Fallon, Physical Review Letters **31**, 690 (1973).
- ¹⁴T. Takizuka and H. Abe, Journal of Computational Physics **25**, 205 (1977).
- ¹⁵T. D. Arber, K. Bennett, C. S. Brady, A. Lawrence-Douglas, M. G. Ramsay, N. J. Sircombe, P. Gillies, R. G. Evans, H. Schmitz, A. R. Bell, and C. P. Ridgers, Plasma Physics and Controlled Fusion 57, 113001 (2015).
- ¹⁶S. I. Braginskii, Soviet Physics JETP **6**, 358 (1958).
- ¹⁷S. Chandrasekhar, The Astrophysical Journal **97**, 255 (1943).
- $^{18}R.\ S.\ Cohen,\ L.\ Spitzer,\ \ and\ P.\ M.\ Routly,\ Physical\ Review\ 80,\ 230\ (1950).$
- ¹⁹L. Spitzer and R. Härm, Physical Review **89**, 977 (1953).
- ²⁰B. A. Trubnikov, Reviews of Plasma Physics **1**, 105 (1965).
- ²¹N. A. Krall and A. W. Trivelpiece, *Principles of plasma physics*, International series in pure and applied physics (McGraw-Hill, 1973).

- ²²P. M. Bellan, Fundamentals of Plasma Physics (Cambridge University Press, Cambridge, 2006).
- ²³K. Nanbu, Physical Review E **55**, 4642 (1997).
- ²⁴J. Connor and R. Hastie, Nuclear Fusion **15**, 415 (1975).
- ²⁵M. Landreman and D. R. Ernst, Journal of Computational Physics **243**, 130 (2013).
- ²⁶Y. Zhang, S. Pree, and P. M. Bellan, Nature Astronomy (2023), 10.1038/s41550-023-01941-x.
- ²⁷E. E. Trofimovich and V. P. Krainov, Sov. Phys. JETP **75**, 27 (1992).
- ²⁸D. Nicholson, *Introduction to plasma theory* (Wiley, 1983).
- ²⁹R. Goldston and P. H. Rutherford, *Introduction to Plasma Physics*, 0th ed. (Institute of Physics, Bristol, UK, 1995).
- ³⁰G. Lantoine and R. P. Russell, Celestial Mechanics and Dynamical Astronomy **109**, 333 (2011).
- ³¹J. B. Boffard, G. A. Piech, M. F. Gehrke, L. W. Anderson, and C. C. Lin, Physical Review A **59**, 2749 (1999).
- ³²C. Fa-Yin and S. Bing-Ren, Chinese Physics **16**, 3458 (2007).
- ³³K. Miyamoto, *Plasma physics for nuclear fusion, Revised Edition* (MIT Press, Cambridge MA, 1989).
- ³⁴H. Knoepfel and D. Spong, Nuclear Fusion **19**, 785 (1979).
- ³⁵B. N. Breizman, P. Aleynikov, E. M. Hollmann, and M. Lehnen, Nuclear Fusion **59**, 083001 (2019).
- ³⁶K.-B. Chai, X. Zhai, and P. M. Bellan, Physics of Plasmas **23**, 032122 (2016).